frontiers | Frontiers in Earth Science

TYPE Original Research
PUBLISHED 28 July 2025
DOI 10.3389/feart.2025.1567728

OPEN ACCESS

EDITED BY
Michel Grégoire,
UMR5563 Géosciences Environnement Toulouse (GET), France

REVIEWED BY
Xiaodong Deng,
China University of Geosciences Wuhan, China
Jing Sun,
College of Geosciences, China University of Petroleum, China

*CORRESPONDENCE
Wang Denghong,
wangdenghong@vip.sina.com
Zhang Juquan,
juquan1983@163.com

RECEIVED 28 January 2025
ACCEPTED 30 June 2025
PUBLISHED 28 July 2025

CITATION
Yanan J, Denghong W, Juquan Z and Long Z (2025) Controlling factors of the metallogenic intensity in Han–Xing-type skarn iron deposits: insights from trace elements in magmatic magnetite.
Front. Earth Sci. 13:1567728.
doi: 10.3389/feart.2025.1567728

Controlling factors of the metallogenic intensity in Han–Xing-type skarn iron deposits: insights from trace elements in magmatic magnetite

Jin Yanan[1,2], Wang Denghong[2]*, Zhang Juquan[3,4]* and Zhang Long[5]

[1]College of Earth and Planetary Sciences, Chengdu University of Technology, Chengdu, China, [2]MNR Key Laboratory of Metallogeny and Mineral Assessment, State Key Laboratory of Deep Earth and Mineral Exploration, Institute of Mineral Resources, Chinese Academy of Geological Sciences, Beijing, China, [3]College of Earth Sciences, Hebei Geo University, Shijiazhuang, China, [4]Hebei Key Laboratory of Strategic Critical Mineral Resources, Hebei GEO University, Shijiazhuang, China, [5]Shandong Provincial No.4 Institute of Geological and Mineral Survey, Weifang, China

The Handan–Xingtai region is one of the important production areas of skarn-type iron deposits in China. The magmatic rocks associated with iron mineralization in this region are predominantly intermediate-basic and intermediate-felsic in composition, and different intrusive complexes exhibit distinct metallogenic intensity. This study focuses on the major and trace-element geochemical analysis of magnetite in the Kuangshan and Fushan complexes to explore the controlling factors of the metallogenic intensity of Han–Xing-type skarn iron deposits. Through partial least squares discriminant analysis (PLS-DA) and orthogonal partial least squares discriminant analysis (OPLS-DA), it has been found that magnetite in the Kuangshan complex is enriched in Ti, Si, Cu, and Mn but depleted in V, Cr, Ni, Co, Ga, Al, and Mg. In contrast, magnetite in the Fushan complex is characterized by high concentrations of Co, Ni, Cr, and V. The results of mineral geochemical analyses indicate that the Kuangshan complex experienced plagioclase fractional crystallization and was formed in a low-temperature, high-oxygen fugacity environment, derived from cognate magma through crystallization differentiation. The Fushan complex is the product of non-cognate magma evolution and was formed in a low-oxygen fugacity environment. Therefore, the chemical composition of magnetite can serve as an effective tool for studying the enrichment mechanism of skarn-type iron deposits. At the same time, a high fO_2 environment is conducive to the precipitation and migration of Co from magnetite, which is more favorable for the formation of associated Co deposits during the later sulfide stage.

KEYWORDS

magnetite, magma evolution, oxygen fugacity, Handan–Xingtai area, partial least squares discriminant analysis and orthogonal partial least squares discriminant analysis

1 Introduction

The Han–Xing (Handan-–Xingtai) region is one of the most important skarn-type iron ore producers in eastern China. Currently, more than 100 deposits have been discovered, with proven reserves of approximately 1 billion tons (Shen et al., 2015; Deng et al., 2015; Wen et al., 2020). However, there are still many controversies about ore genesis, mainly focusing on whether the metallogenic methods involve contact metasomatism or "ore pulp" penetration and whether the ore-forming materials are from multiple-sources or a single source (Liu, 1984; Niu et al., 1995; Li and Santhosh, 2013; Shen et al., 2013).

There are significant differences in the quantity and scale of deposits formed by different complexes in the Han–Xing region. The key to determining the controlling factors of mineralization is to analyze the genesis, evolution, and physicochemical conditions of these complexes with different metallogenic intensities. Sun et al. (2015); Sun (2016); Sun et al. (2019) studied the Hongshan complex and proposed that the main factors affecting metallogenic intensity are the contribution of continental crust and the magmatic oxidation state. However, the Hongshan complex is mainly composed of syenite, which is the only barren complex in the Han–Xing area. The physicochemical differences between the Hongshan complex and the ore-forming complex reflect the lithology differences rather than the key controlling factors of mineralization.

Magnetite is the primary ore mineral in the Handan–Xingtai region, and it is consistently found in magmatic, sedimentary, and metamorphic rocks. The chemical composition of magnetite is influenced by various factors, including temperature, pressure, oxygen fugacity, sulfur fugacity, paragenetic minerals, and the surrounding rocks. Therefore, the analysis of the major and trace elements in magnetite holds significance for determining the genesis and evolution of the Han–Xing-type skarn iron deposit (Buddington and Lindsley, 1964; Ramdohr, 1980; Dupuis and Beaudoin, 2011; Dare et al., 2012; Dare et al., 2014; Nadoll et al., 2015).

This study collected fresh rock samples with diverse lithologies from the Kuangshan complex with strong metallogenic intensity and from the Fushan complex with weak metallogenic intensity. Drawing on multivariate statistical methods such as partial least squares discriminant analysis (PLS-DA) and orthogonal partial least squares discriminant analysis (OPLS-DA) methods, the differences in magnetite between the complexes with different metallogenic intensities were identified, the reasons for the formation of the differences were analyzed, and then the key restrictive factors controlling the metallogenic intensity were explored.

2 Regional geology

The Han–Xing region is located in the southwest of Hebei Province, China, and is part of the Mesozoic southern Taihang Mountain tectonic–magmatic belt in the central North China Craton. The study region covers an area of 350 km^2 and is separated by the Taihang Mountain piedmont fault and the Xibaiyu deep fault in the east and west (Shen et al., 2013; Zhang et al., 2014; Deng et al., 2015; Jin et al., 2015; Sun et al., 2015). The Han–Xing-type skarn iron deposits are characterized by high ore grade and large reserves, and they are the main sources of high-grade iron ore in China (Chen et al., 2004; Wang et al., 2006; Qian and Hermann, 2010; Xu et al., 2010; Jin et al., 2015; Huo et al., 2019; Zhang et al., 2020). The Mesozoic magmatic activities in the region are related to the destruction of the North China Craton caused by the subduction of the Paleo-Pacific Plate (Li et al., 2013; Zhu et al., 2012; Li et al., 2013; Zhang et al., 2014; Shen et al., 2015; Wu et al., 2019; Figure 1A).

The distribution of intrusive rocks in this area is primarily controlled by NNE- and EW-trending faults. According to the distribution characteristics of the intrusive rocks, the whole region is divided into three magmatic rock belts and eight complexes (Zhu et al., 2012; Li and Santhosh, 2013; Li et al., 2013; Zhang et al., 2014; Wu et al., 2019; Figure 1B). The three magmatic rock belts are the western, central, and eastern magmatic rock belts, among which the central magmatic rock belt is the most important and significant, where the majority of the large and medium-sized deposits are distributed. The magmatic rocks mainly consist of gabbro diorite, hornblende diorite, diorite, diorite porphyrite, monzonite, and syenite, with emplacement ages ranging from 125 Ma to 135 Ma (Chen et al., 2008; Li et al., 2013; Shen et al., 2013; Zhang et al., 2014; Sun et al., 2019).

According to previous studies, the central metallogenic belt may be primarily influenced by the Wu'an fault basin, with a quantity of iron deposits developed along its "basin edge" (Cai et al., 1987; Zheng et al., 2006; Shen et al., 2013; Li et al., 2013). Mg-skarn-type iron deposits are produced in the contact zone between diorite–monzonite and carbonatite surrounding rocks, and more than 95% of skarn-type iron deposits are closely related to the evaporite layer of the Middle Ordovician and are located near the contact zone of intrusive rocks of the Middle Ordovician Majiagou, Cixian, and Fengfeng formations (Li et al., 2013; Zhang et al., 2015; Figure 1B).

The Kuangshan complex is situated in the middle section of the central metallogenic belt, and it serves as a significant ore-concentrated area in the Han–Xing region, with an exposed area of approximately 45 km^2. In this region, the Xishimen deposit is the largest iron deposit currently under exploitation. The orebody mainly occurs in layered formations and extends in the SE direction. Mineralization is from the Early Cretaceous Epoch. The intrusive rocks associated with iron mineralization include monzonite, diorite, diorite–porphyrite, and syenodiorite. The zircon U–Pb age indicates that the magmatic intrusive time of the Kuangshan complex was 127–133 Ma (Chen et al., 2008; Wei, 2011; Sun et al., 2015; Sun, 2016; Li. 2019; Figure 2A). The Fushan complex is located in the western metallogenic belt, and the exposed area is larger than the Kuangshan complex; the area is approximately 58 km^2. The surrounding rocks mainly expose the Cambrian and Ordovician carbonate strata (Shen et al., 2015). In the Fushan complex, the crosscut relationships are obvious. The hornblende diorite is enclosed within the diorite, whereas the syenite intersects through both the previously mentioned rock types. The zircon U–Pb age indicates that the magmatic intrusive time of the Fushan complex was 123–131 Ma, which was formed contemporaneously with the Kuangshan complex—and slightly earlier than—the Kuangshan complex (Peng et al., 2004; Chen et al., 2008; Xu et al., 2010; Wang et al., 2006; Deng et al., 2015; Shen et al., 2015; Sun, 2016; Li, 2019; Figure 2B).

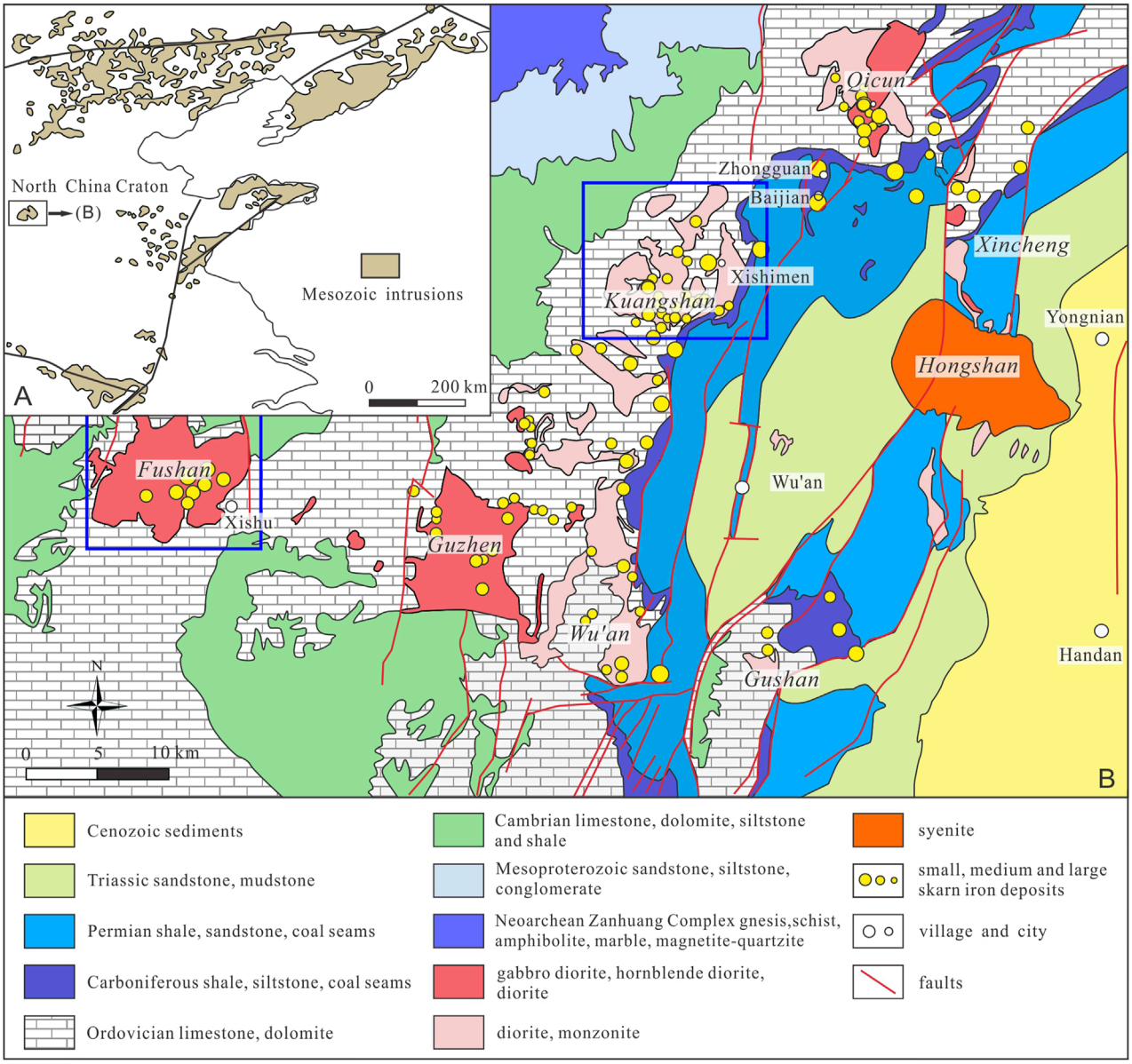

FIGURE 1
(A) Geological map of the North China Craton (revised from Wu et al., 2019). **(B)** Geological map of the Han–Xing region (revised from Zhang et al., 2015).

3 Sampling and analytical methods

3.1 Sample description

The samples collected from the Kuangshan and Fushan complexes are detailed in Table 1. Four representative samples were collected from the Kuangshan complex, namely, diorite (KS1), diorite (KS2), syenodiorite (KS3), and monzonite (KS4). The diorite is gray with a medium- to fine-grained texture and is primarily composed of plagioclase (65 vol%), amphibole (30% vol%), and K-feldspar (5% vol%). The main accessory minerals include magnetite, zircon, apatite, and sphene, and ilmenite was not found. Magnetite with apatite inclusions was associated with amphibole and sphene (Figures 3A–C). Diorite is gray and is mainly composed of plagioclase (70 vol%), amphibole (25 vol%), and K-feldspar (5% vol%). The accessory minerals consist of magnetite, apatite, zircon, and sphene (Figures 3D–F). The syenodiorite is grayish-white in color, with medium- to fine-grained texture and a massive structure, and is mainly composed of plagioclase (60 vol%), K-feldspar (30 vol%), and amphibole (10 vol%). Ilmenite was replaced by sphene (Frost and Lindsley, 1991; Figures 3G–I). The monzonite is pale pink in color and consists of K-feldspar (50 vol%), plagioclase (40 vol%), and amphibole (10 vol%). The accessory minerals are magnetite, apatite, zircon, and sphene. Under backscattered electron (BSE) imaging, the magnetite has a smooth surface, and ilmenite occurs as exsolution lamellae (Figures 3J–L).

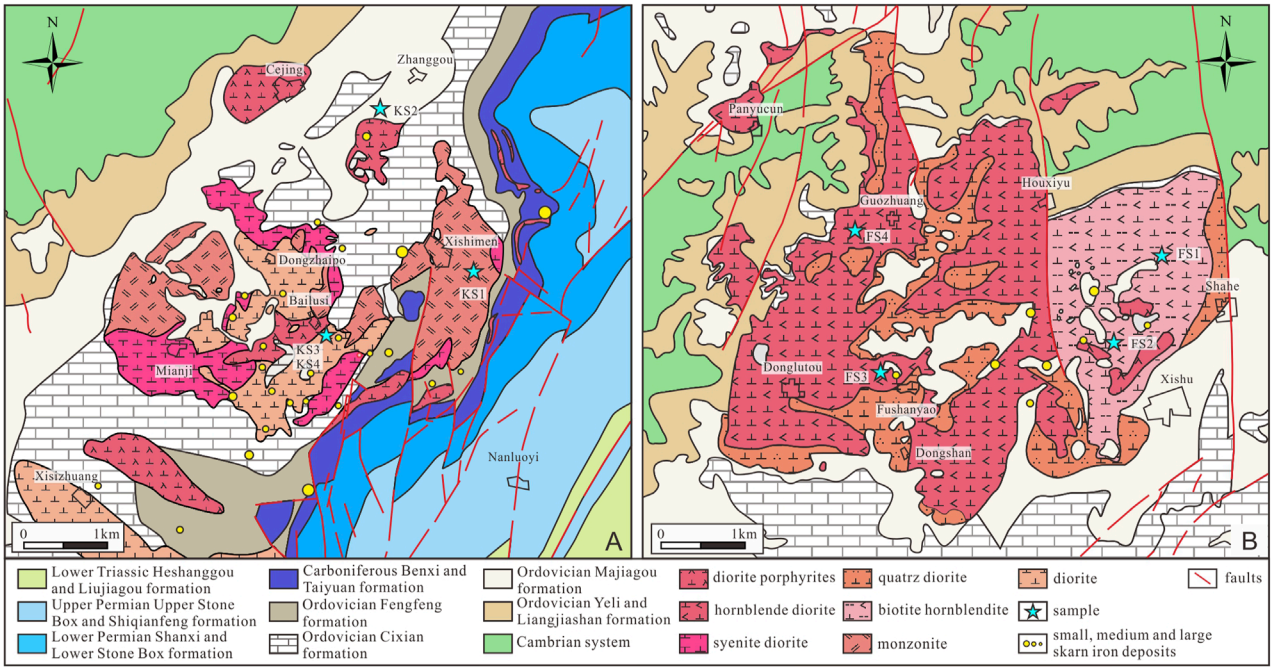

FIGURE 2
(A) Geological map of the Kuangshan complex (revised from Jiang et al., 2020). **(B)** Geological map of the Fushan complex (revised from Shen et al., 2015).

TABLE 1 Characteristics of the samples from the Fushan and Kuangshan complexes.

No.	Complex	Lithology	Texture	Main mineral	Accessory mineral
KS1	Kuangshan	Diorite	Medium- to fine-grained texture	Pl (65%) + Amp (30%) + Kfs (5%)	Mag + Ap + Zrn
KS2	Kuangshan	Diorite	Medium- to fine-grained texture	Pl (70%) + Amp (25%) + Kfs (5%)	Mag + Ap + Zrn
KS3	Kuangshan	Syenodiorite	Medium- to fine-grained texture	Pl (60%) + Kfs (30%) + Amp (10%)	Mag + Ap + Zrn
KS4	Kuangshan	Monzonite	Medium- to coarse-grained texture	Kfs (50%) + Pl (40%) + Amp (10%)	Mag + Ap + Sph + Zrn
FS1	Fushan	Porphyritic hornblende diorite	Porphyritic texture	Pl (60%) + Amp (35%) + Cpx (5%)	Mag + Ap + Sph + Zrn
FS2	Fushan	Hornblendite	Hypidiomorphic-granular texture	Pl (60%) + Amp (40%)	Mag + Ap + Zrn
FS3	Fushan	Diorite	Medium- to fine-grained texture	Pl (75%) + Amp (25%)	Mag + Ap + Zrn
FS4	Fushan	Monzonite	Medium- to coarse-grained texture	Pl (50%) + Kfs (35%) + Amp (15%)	Mag + Ap + Sph + Zrn

The four representative rock samples collected from the Fushan complex consist of porphyritic hornblende diorite (FS1), hornblende diorite (FS2), diorite (FS3), and monzonite (FS4). Porphyritic hornblende diorite is ash-black in color, with porphyritic texture and massive structure. It is mainly composed of plagioclase (60 vol%), amphibole (35 vol%), and pyroxene (5 vol%). Under BSE imaging, vanadium-rich magnetite is associated with ilmenite, indicating low fO_2 during the ore-forming process, and a significant amount of V from the parental magma was incorporated into the magnetite lattice (Figures 4A–C). Hornblendite is ash-black in color and has a hypidiomorphic-granular texture, and it is predominantly composed of plagioclase (60 vol%) and amphibole

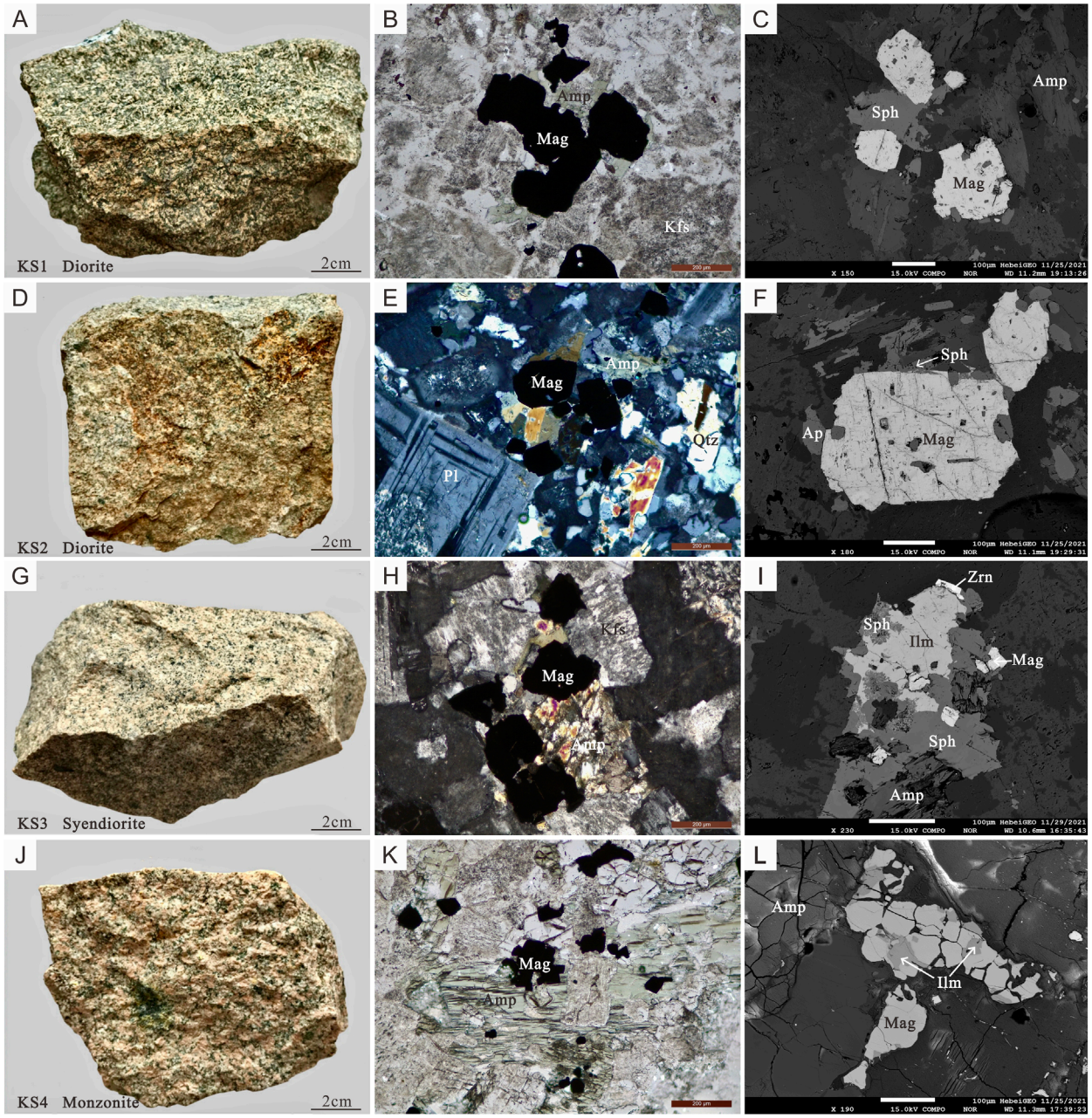

FIGURE 3
Sample features of the Kuangshan complex. **(A)** Diorite (KS1). **(B)** Sample under plane-polarized light (KS1). **(C)** BSE image (KS1). **(D)** Diorite (KS2). **(E)** Sample under cross-polarized light (KS2). **(F)** BSE image (KS2). **(G)** Syenodiorite (KS3). **(H)** Sample under cross-polarized light (KS3). **(I)** BSE image (KS3). **(J)** Monzonite (KS4). **(K)** Sample under plane-polarized light (KS4). **(L)** BSE image (KS4). Mineral assemblages include magnetite (Mag), ilmenite (Ilm), amphibolite (Amp), apatite (Ap), sphene (Sph), quartz (Qtz), and zircon (Zrn).

(40 vol%), where magnetite occurs as euhedral grains wrapped in amphibole (Figures 4D–F). The diorite is grayish-white in color and is mainly composed of plagioclase (75 vol%) and amphibole (25 vol%). The accessory minerals include magnetite, sphene, and apatite. The magnetite displays a smooth surface and is associated with amphibole and sphene (Figures 4G–I). The monzonite is light gray in color and is mainly composed of plagioclase (50 vol%), K-feldspar (35 vol%), and amphibole (15 vol%). Magnetite can be seen coexisting with apatite (Figures 4J–L).

3.2 Analytical methods

3.2.1 EPMA analyses

Based on comprehensive petrographic studies, we analyzed the major element in magnetite from the Kuangshan and Fushan complexes and obtained a total of 229 EPMA data points. The analysis was carried out in the EPMA Laboratory of Hebei GEO University using the JEOL JXA-8230 electron probe micro-analyzer (EPMA); the operating conditions were 15 kV accelerating voltage

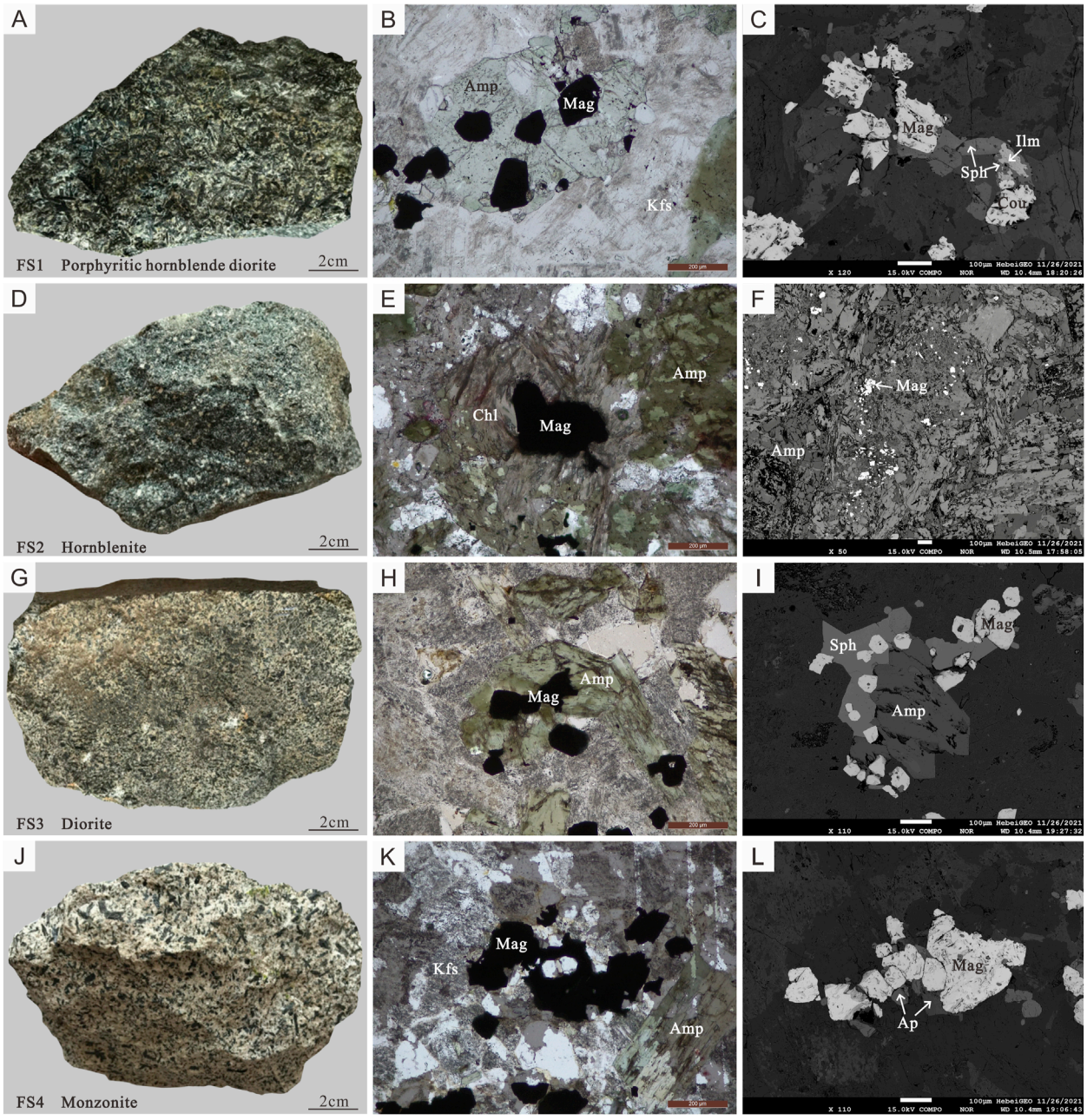

FIGURE 4
Sample features of the Fushan complex. **(A)** Porphyritic hornblende diorite (FS1). **(B)** Sample under plane-polarized light (FS1). **(C)** BSE image (FS1). **(D)** Hornblendite (FS2). **(E)** Sample under plane-polarized light (FS2). **(F)** BSE image (FS2). **(G)** Diorite (FS3). **(H)** Sample under plane-polarized light (FS3). **(I)** BSE image (FS3). **(J)** Monzonite (FS4). **(K)** Sample under plane-polarized light (FS4). **(L)** BSE image (FS4). Mineral assemblages include magnetite (Mag), ilmenite (Ilm), amphibolite (Amp), apatite (Ap), sphene (Sph), zircon (Zrn), and coulsonite (Cou).

and a beam current of 20 nA, and the beam spot diameter ranged from 2 μm to 5 μm.

3.2.2 LA–ICP–MS analyses

The trace element composition of magnetite was analyzed by laser ablation–inductively coupled plasma–mass spectrometry (LA–ICP–MS). The analysis was completed in the Hebei Key Laboratory of Strategic Critical Mineral Resources, Hebei GEO University. The laser ablation (LA) system used is Australian RESOlution-LR (a high energy ArF_2 excimer laser ablation system), equipped with a Laurin Technic S155 Sample Cell and GeoStarμGISTM software. The mass spectrometer (ICP–MS) is a Thermo Scientific iCAP RQ plasma mass spectrometer. The laser beam spot diameter is 29 μm, the laser energy density is 3 J/cm^2, and the ablation frequency is 8 Hz. A 10-s gap was applied before ablation, followed by 40 s of ablation and a 20 s purge after ablation was completed. The carrier gas is high-purity helium, and the gas flow rate is 0.6 L/min. The auxiliary gas is Ar gas, and the

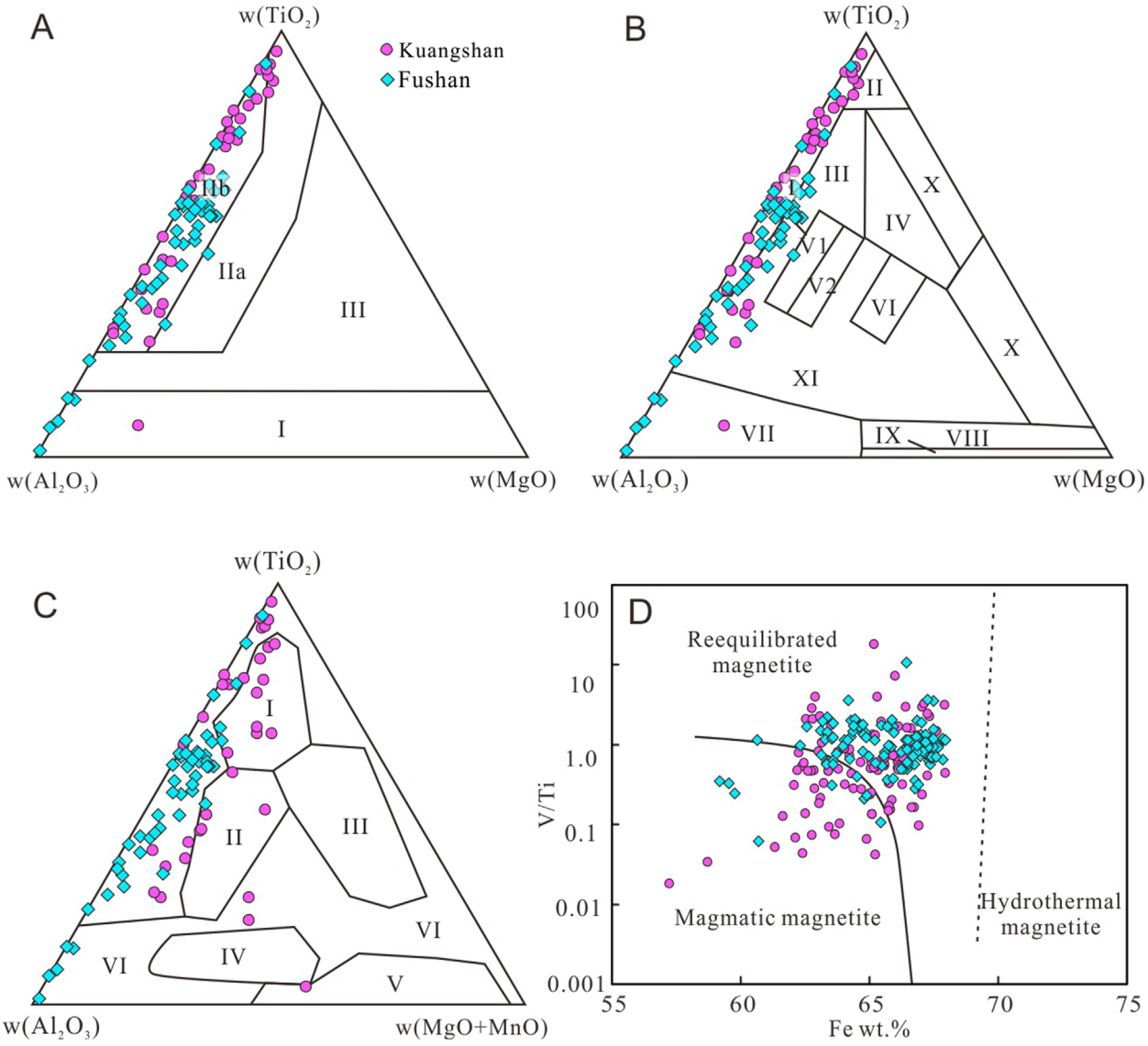

FIGURE 5
Diagrams of the genetic discrimination of magnetite. **(A) (I)**. Sedimentary metamorphic-contact metasomatic magnetite, IIa. Ultrabasic–basic–intermediate igneous magnetite, IIb. Acid–alkaline igneous magnetite (after Chen et al., 1987). **(B) (I)**. Granite field (acidic rock, pegmatite), II. basalt field (tholeiite, *etc.*), III. gabbro field (gabbro, peridotite, monzonite, anorthosite-accessory mineral, and iron ore), IV. peridotite field (periclotite, dunite, pyroxenite, *etc.*, accessory mineral, and iron ore), V_1. amphibolite field (including clinopyroxenite), V_2. diorite field, VI. kimberlite field, VII. hydrothermal type and calc-skarn type (hypogene hypothermal type above the dashed line and hydrothermal plus skarn type below the dashed line), VIII. hydrothermal type and magnesium skarn type (including hypothermal type and hydrothermal metasomatic type, partly), IX. sedimentary metamorphic, hydrothermal overlapping type, X. carbonatite field (including X_1 area-related basic rock and X_2 area-related wall rock alteration), and XI. transitional field (after Wang, 1987). **(C) (I)**. Accessory mineral type, II. Magma immiscible titanomagnetite type, III. Volcanic type, IV. Contact metasomatic type, V. Skarn type, VI. Sedimentary metamorphic type (after Liu, 1984). **(D)** Diagram of Fe (wt%) vs. (V/Ti) for magnetite (after Wen et al., 2020).

gas flow rate is 0.8 L/min. The working conditions of the mass spectrometer are as follows: cooling gas (Ar) 14 L min^{-1}, auxiliary gas (Ar) 0.8 L min^{-1}, sample gas (Ar) 0.8 L min^{-1}, and blank acquisition time 10 s.

3.2.3 Statistical methods

The PLS-DA is currently widely used in various disciplines and can be used to perform regression modeling on large amounts of data when there are multiple correlations between independent variables. Huang (2018) studied the trace-element composition of magnetite and hematite in IOCG- and IOA-type deposits by PLS-DA, and it was found that the trace-element composition of iron oxides is controlled by oxygen fugacity, temperature, symbiotic minerals, and parent rocks (Huang et al., 2018). In this study, classified and multivariate statistical analysis was used to analyze the differences in magnetite composition between complexes with strong and weak metallogenic intensity.

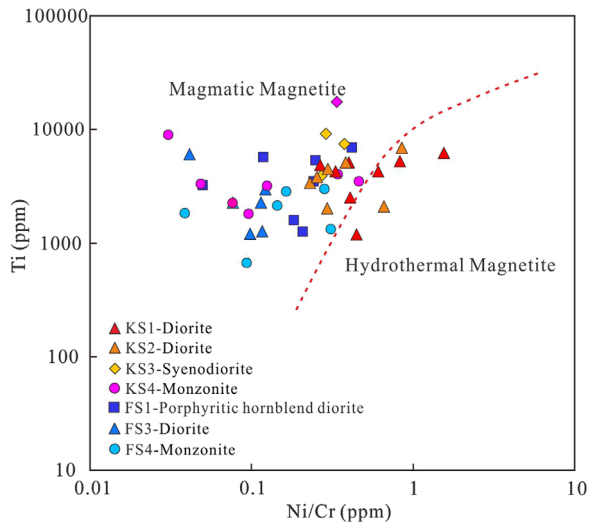

FIGURE 6
Diagram of Ti vs. (Ni/Cr) in magnetite (after Dare et al., 2014).

OPLS-DA can concentrate classification information primarily into one principal component, thus simplifying the model and enhancing the analytical capability and effectiveness, further obtaining inter-group difference information. The OPLS-DA analysis incorporates both S-plot and VIP score plots, wherein variables with VIP >1 are identified as decisive factors within the model.

4 Result

4.1 Major elements of magnetite

The major element concentrations of magnetite in the Kuangshan and Fushan complexes are detailed in Supplementary Table S1. The TiO_2 concentration in the Kuangshan complex (0.01–10.53 *wt*%, average 0.83 *wt*%) is higher than that in the Fushan complex (TiO_2 0.02%–17.21 *wt*%, average 0.48 *wt*%), while V_2O_3 (0.05–0.31 *wt*%, average 0.16 *wt*%) and Cr_2O_3 (0–0.50 *wt*%, average 0.08 *wt*%) concentrations are lower than those in the Fushan complex (V_2O_3 0.09–0.33 *wt*%, average 0.21 *wt*%; Cr_2O_3 0.02–6.62 *wt*%, average 0.71 *wt*%).

The TiO_2–Al_2O_3–MgO, TiO_2–Al_2O_3–MgO + MnO, and Fe (wt%) vs. V/Ti diagrams show the differences in the composition characteristics of magnetite with different genetic types (Liu, 1984; Chen et al., 1987; Wang, 1987; Wen et al., 2020). The projection results of 229 major element data points of magnetite obtained through EPMA indicate that most magnetite falls within the range of acidic–alkaline magmatic magnetite, which is consistent with the lithology of the samples (Figure 5A). The magnetite from the Kuangshan complex is predominantly distributed in the granite region, mostly belonging to accessory mineral and magmatic types, while individual magnetite samples from the Fushan complex are distributed in the hydrothermal type, Ca-skarn type, and transition area (Figures 5B, C). The Fe (wt%) vs. (V/Ti) diagram demonstrates that all magnetite samples are situated within the re-equilibrated and magmatic magnetite regions, exhibiting a continuous compositional trend (Figure 5D). In this study, the majority of samples are well preserved, and the tested magnetite samples are encapsulated by other minerals, thereby minimizing their interaction with fluids. These characteristics suggest that the magnetite crystallized within a water-rich magmatic system.

4.2 Trace elements of magnetite

The trace elements of magnetite from the investigated samples are detailed in Supplementary Table S2. A total of 48 data points were obtained. Due to the high number of inclusions in the FS2 sample from the Fushan complex, the data accuracy was compromised, rendering the trace-element analysis applicable only to the remaining three sample groups.

The concentrations of Ti, Mg, Mn, Al, Cr, V, Ni, Co, Zn, and Ga in magnetite are crucial parameters for determining the physicochemical conditions of magnetite formation, providing significant insights into fluid evolution, ore-forming processes, and ore genesis (Ye, 1982; Nadoll et al., 2012; Nadoll et al., 2014). Magnetite from the Kuangshan complex exhibits higher Ti concentration (1,190.32–9,215.91 ppm, average 4,870.22 ppm) and Mn concentration (173.46–6,351.08 ppm, average 1,328.44 ppm) than that from the Fushan complex. Conversely, the concentrations of V (1915.34–2,860.01 ppm, average 2,353.02 ppm), Cr (119.62–2,533.38 ppm, average 712.10 ppm), Co (18.06–102.89 ppm, average 60.20 ppm), Ni (44.23–129.09 ppm, average 70.07 ppm), and Ga (27.82–52.01 ppm, average 43.47 ppm) are significantly lower than those in the Fushan complex. These characteristics align with the results obtained from the EPMA analysis.

The concentrations of siderophile elements such as Ti, V, Cr, and Ni effectively distinguish magmatic magnetite from hydrothermal magnetite (Nielsen et al., 1994; Ewart and Griffin, 1994; Li et al., 2018; Javad et al., 2019; Ghaz et al., 2019). These elements' concentrations in magnetite are primarily influenced by temperature, oxygen fugacity, and partition coefficients. Conversely, the concentrations of lithophile elements such as Mg, Al, Mn, and Ca are relatively low (Dora et al., 2020; Chen et al., 2020). The Ti–Ni/Cr diagram of magnetite indicates that, except for the hydrothermal characteristics exhibited by magnetite in the diorite of the Kuangshan complex, the majority of the magnetite samples in this study exhibit chemical compositions that are typical of magmatic magnetite (Figure 6).

The element distribution coefficient serves as the primary factor influencing the incorporation of trace elements from the melt into magnetite (Dare et al., 2012; Dare et al., 2014). Variations in trace-element concentrations can be leveraged to analyze the formation environment of magnetite and reflect the magmatic evolution process. Comparative boxplot analysis of magnetite compositional characteristics across various metallogenic complexes and lithologies reveals that the Kuangshan complex is enriched in Cu, Mn, Pb, Ti, Zn, and Zr, whereas the Fushan complex is enriched

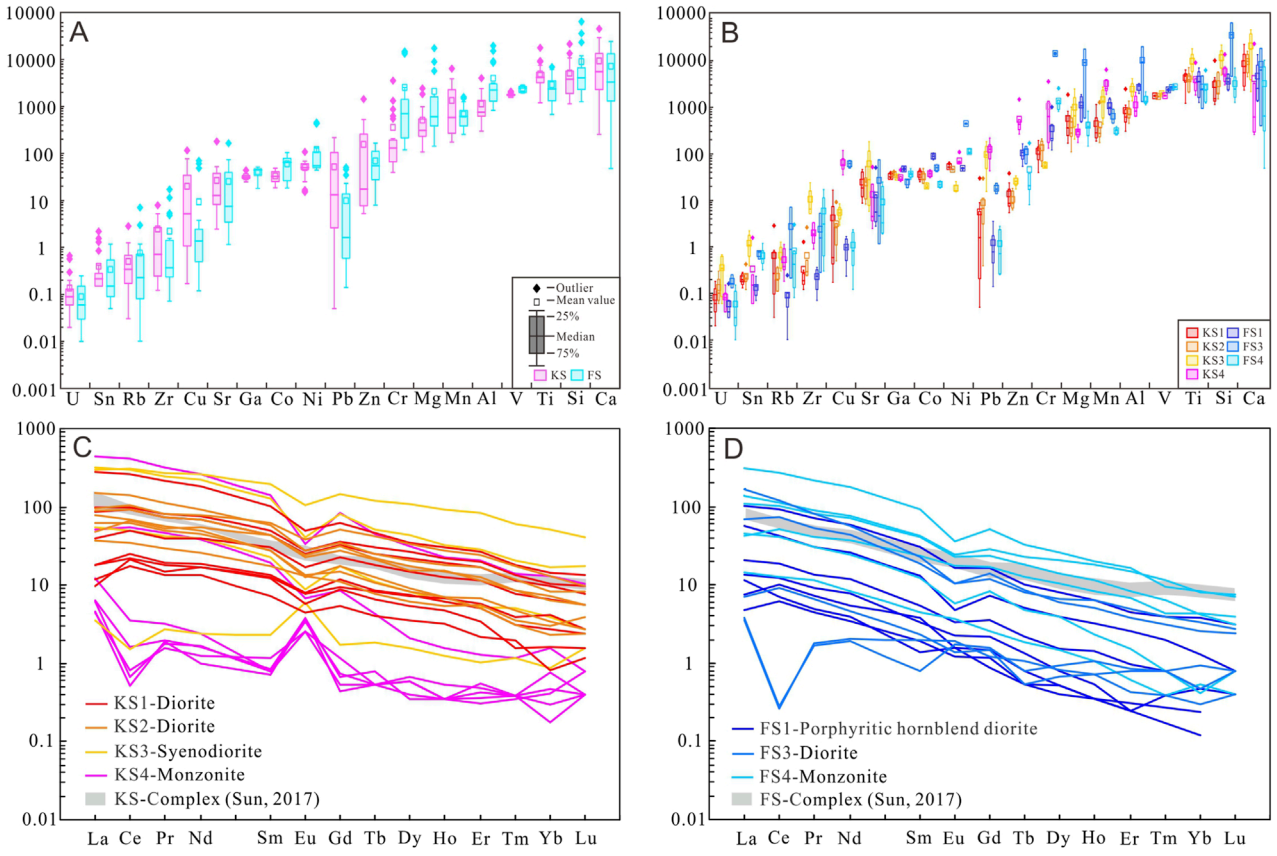

FIGURE 7
Diagram of magnetite LA–ICP–MS data. **(A–B)** Trace-element concentrations in magnetite from the Kuangshan and Fushan complex samples are shown as box and whisker plots. **(C)** Chondrite-normalized REE distribution patterns of Kuangshan complex magnetite. **(D)** Chondrite-normalized REE distribution patterns of Fushan complex magnetite. The chondrite REE values are from Sun and Mcdonough, 1989.

in Al, Co, Cr, Mg, Ga, Sn, Ni, and V (Figure 7A). The significant enrichment of Ti in the syenodiorite (KS3) of the Kuangshan complex suggests that the magnetite in this lithology formed at relatively high temperatures. In contrast, the continuous variation in Ti concentrations in the Fushan complex, transitioning from basic to intermediate lithologies and from relative enrichment to gradual depletion, indicates a progressive temperature decrease during magma migration and continuous crystallization of magnetite (Figure 7B).

4.3 Rare-earth elements of magnetite

According to the chondrite-normalized rare-earth element (REE) distribution patterns of magnetite, both the Kuangshan and Fushan complexes exhibit right-inclined REE characteristics, indicating LREE enrichment and HREE depletion. In the Kuangshan complex, ΣLREE was 2.39–535.6 ppm (average 119.62 ppm) and ΣHREE was 0.98–227.46 ppm (average 36.05 ppm). In the Fushan complex, ΣLREE was 0.98–362.72 ppm (average 64.67 ppm) and ΣHREE was 0.51–55.23 ppm (average 12.27 ppm) (Figures 7C, D).

The monzonite sample (KS4) from the Kuangshan complex displays a distinct magnetite REE distribution pattern compared to other samples, characterized by pronounced positive Eu anomalies. Eu anomalies are closely associated with plagioclase separation crystallization (Bau, 1991; Klinkhammer et al., 1994; Hass et al., 1995). Temperature and fO_2 also significantly influence Eu anomalies, with high temperature and an oxidation environment being critical factors for the formation of positive Eu anomalies (Hass et al., 1995; Yang et al., 2007). The whole-rock REE distribution patterns do not exhibit significant Eu and Ce anomalies. However, KS4 displays both positive Eu and negative Ce anomalies, suggesting that the formation occurred in a relatively oxidized environment without significant plagioclase separation crystallization (Ding et al., 2003; Zhao et al., 2007; Hao et al., 2011; Yang et al., 2022; Figures 7C, D).

4.4 PLS-DA and OPLS-DA results of magnetite

The PLS-DA statistical analysis revealed that approximately one-third of the samples in different ore-bearing complexes exhibited overlapping characteristics, although the overall separation trend remained relatively distinct (Figure 8A). Loading plot analysis indicated that magnetite in the strong metallogenic complex was enriched in TiO_2 and SiO_2, whereas magnetite in the weak

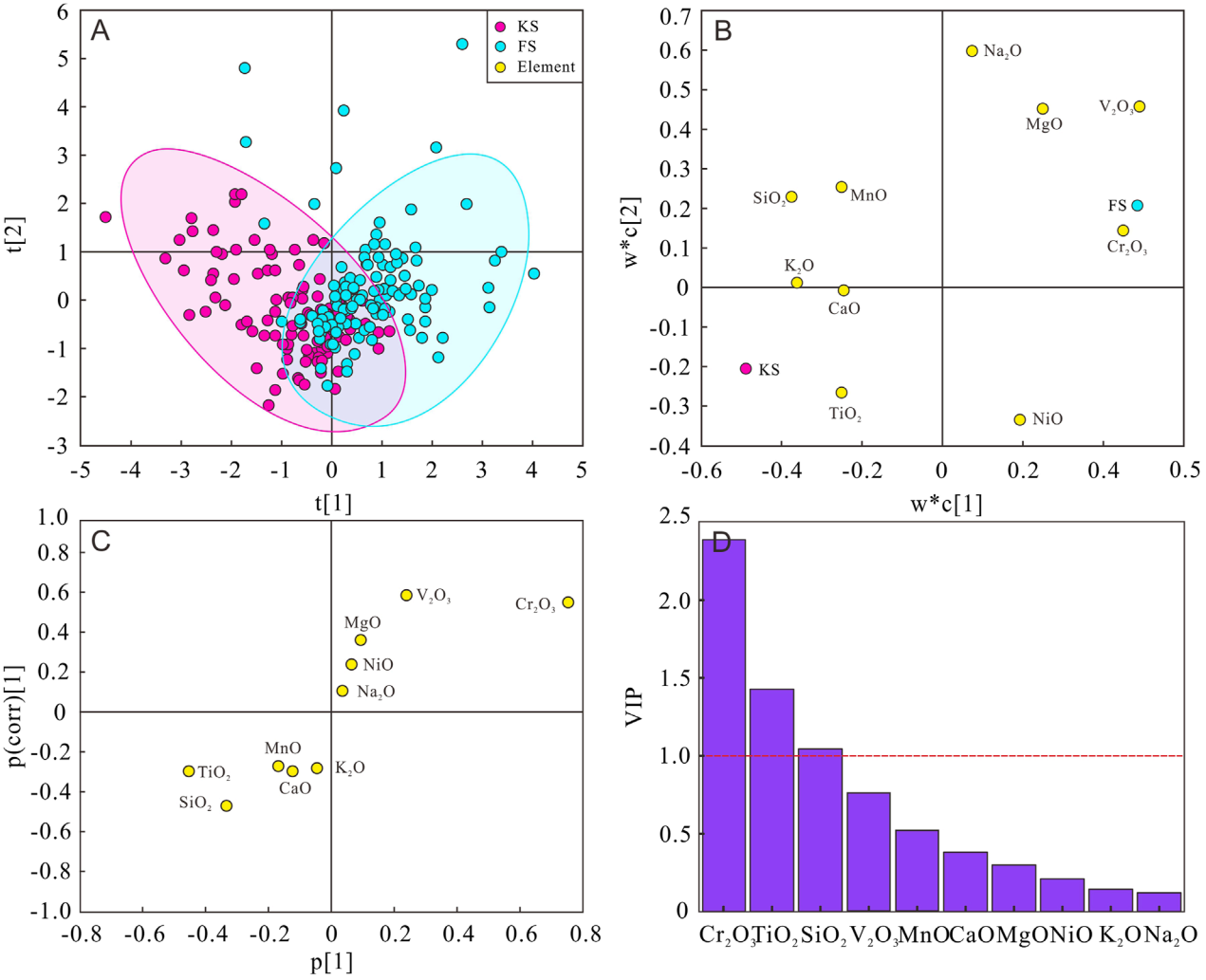

FIGURE 8
PLS-DA and OPLS-DA of magnetite EPMA data in the Kuangshan and Fushan complexes. **(A)** Score plot. **(B)** Loading plot. **(C)** S-plot. **(D)** VIP score plot.

metallogenic complex was predominantly enriched in V_2O_3 and Cr_2O_3 (Figure 8B). Through a comprehensive analysis of the S-plot and VIP score plot, Cr_2O_3, TiO_2, and SiO_2 were identified as the key elements characterizing the compositional features of magnetite models in complexes with varying metallogenic intensities, with all VIP > 1 (Figures 8C, D).

The LA–ICP–MS analysis method offers comprehensive elemental information for magnetite, particularly facilitating the effective detection of trace elements. This study selected 18 elements with significant indicative value for magnetite, including Si, Ti, Mg, Mn, Zn, Cr, V, Ni, Co, Sn, and Ga, for the PLS-DA and OPLS-DA model analysis. The results indicate that magnetite in the Kuangshan complex exhibits positive correlations with Ti and Cu, whereas magnetite in the Fushan complex shows positive correlations with V, Ga, and Co (Figures 9A, B). The primary characteristic elements distinguishing the metallogenic intensity are Si, Ti, Mg, V, and Cr (VIP>1, Figures 9C, D).

5 Discussion

5.1 Composition identification of magnetite in strong metallogeny

According to the fitting results of the PLS-DA and OPLS-DA models, V_2O_3 + Cr_2O_3 + MgO vs TiO_2 were selected as the most significant characteristic elements for distinguishing between strong and weak metallogeny. A discriminant diagram for strong and weak metallogenic complexes was constructed, which effectively differentiates magnetite in ore-bearing complexes with varying metallogenic intensities. The magnetite in the two complexes converges toward the origin along the Y-axis and X-axis, respectively, indicating a gradual decrease in temperature and an increase in fO_2, thereby enhancing the ore-forming potential. However, significant sample overlap near the origin persists, preventing complete differentiation. Lithological characteristics reveal that these overlapping samples primarily consist of diorite and monzonite from the two complexes (Figure 10).

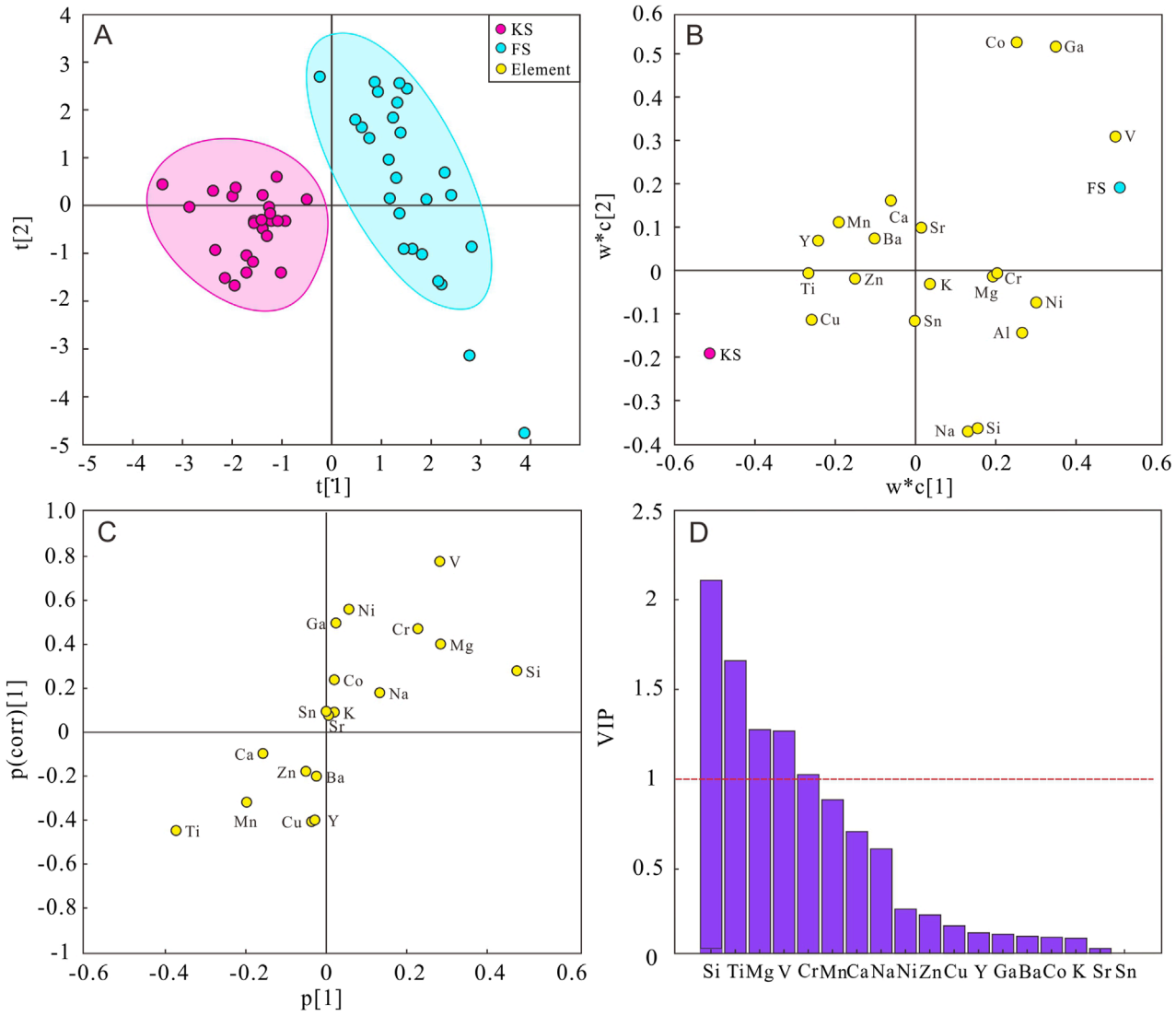

FIGURE 9
PLS-DA and OPLS-DA of magnetite LA–ICP–MS data in the Kuangshan and Fushan complexes. **(A)** Score plot. **(B)** Loading plot. **(C)** S-plot. **(D)** VIP score plot.

Given the inadequacy of the aforementioned discrimination diagram in effectively distinguishing between diorites and monzonites with varying ore-bearing potential, the authors employed PLS-DA and OPLS-DA for regression analysis on samples from overlapping regions. The findings indicated that the primary factor influencing the ore-bearing properties of diorite is the elevated concentrations of V_2O_3 and Cr_2O_3 in the Fushan complex (VIP > 1, Figures 11A–D), whereas the distinctions in monzonite are primarily attributed to elevated SiO_2 and MnO in the Kuangshan complex (VIP > 1, Figures 11E–H).

The discriminant diagram in Figure 10 has been supplemented according to the aforementioned statistical results. The elements influencing the ore-bearing differences in diorite are V_2O_3 and Cr_2O_3, whereas the primary element affecting syenite is SiO_2 (Figure 12). A comparative analysis of magnetite with identical lithologies across diverse complexes was conducted. The findings indicate that iron mineralization is a product of magmatic evolution, with varying magmatic processes leading to differences in ore-forming potential. However, two complexes exhibit an evolutionary trend toward lower temperatures and higher fO_2. Consequently, the compositional characteristics of magnetite serve as a crucial indicator for assessing the ore-forming potential of complexes, providing significant insights into the enrichment mechanisms of Han–Xing-type skarn iron deposits in this region.

The key indicators of metallogenic intensity include V_2O_3, TiO_2, Cr_2O_3, SiO_2, MnO, and MgO. To further explore the evolutionary trends in elemental concentrations, the authors employed violin plots to illustrate the distribution patterns and probability densities of magnetite elements in strong and weak metallogenic intensity complexes. This approach comprehensively illustrates the enrichment patterns of characteristic elements within magnetite. Visualization results reveal that the concentration ranges

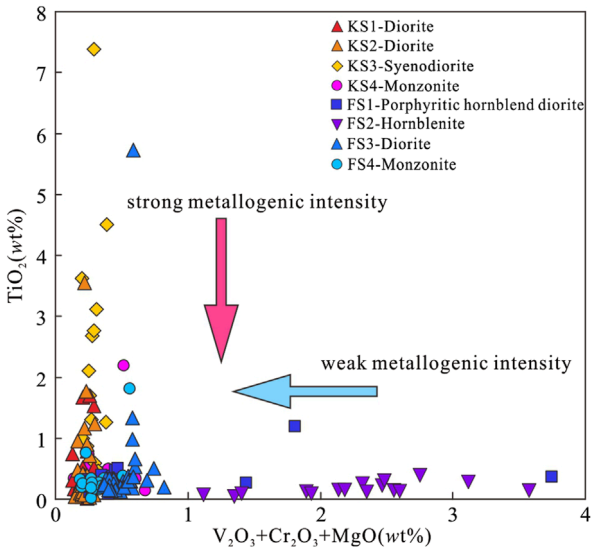

FIGURE 10
Illustration of magnetite metallogenic intensity discrimination.

of SiO_2, TiO_2, and MnO in magnetite from the Kuangshan complex are significantly broader than those of magnetite from the Fushan complex, with only a few samples exhibiting high SiO_2. Conversely, MgO and Cr_2O_3 concentrations remain relatively consistent. In the Fushan complex, V_2O_3 and Cr_2O_3 concentrations are distinctly divided into two intervals, suggesting substantial variations in fO_2 during the magnetite ore-forming process. Additionally, the higher Cr_2O_3 concentration points to a greater contribution of deep-source materials in the Fushan complex (Shen et al., 1979; Qin et al., 2024; Zhang et al., 2018; Figure 13).

Violin plot analysis of trace elements reveals that the concentration ranges of Ti, Mn, Cu, and Ba in the Kuangshan complex are significantly higher than those in the Fushan complex, whereas the concentration of V is notably lower with a restricted distribution range. The elevated Cu concentration in magnetite from the Kuangshan complex may be attributed to the Cu-enriched characteristics of the parent magma. Early crystallized magnetite underwent alteration, leading to variations in trace-element concentrations. Magnetite in the Fushan complex exhibits enrichment in Al, Mg, Cr, V, Ga, and Co, with Ti, Cr, V, and Co displaying two distinct enrichment zones. This indicates a prolonged formation period and significant changes in the mineralization environment (Figure 14).

5.2 Controlling factors of iron metallogeny in the Han–Xing area

Magnetite, serving as the primary accessory mineral in various intrusive rocks and the ore mineral of iron deposits, documents the evolutionary process of the skarn-type iron deposit metallogenic complex and the magma-hydrothermal transformation in the Han–Xing region (Zhang et al., 2014). Previous studies have demonstrated that the Kuangshan and Fushan complexes belong to two distinct metallogenic systems. The partial melting of mantle peridotite was induced by lithospheric thinning, generating basic magma, which subsequently formed these two metallogenic systems through different magma evolutions (Depaolo, 1981; Zhang et al., 2018). The variations in physicochemical conditions within these metallogenic complexes provide invaluable evidence for understanding the factors influencing metallogeny.

Eu and Ce are variable valence elements, and their anomalies reflect the oxidation–reduction environment during diagenesis and mineralization (Schock, 1979; Liu, 1984; Klinkhammer et al., 1994; Chen and Chen, 1990). Beyond the redox condition, the separation crystallization of plagioclase can induce significant Eu anomalies (Yang et al., 2007; Zhao et al., 2007). Chondrite-normalized spider diagrams reveal that magnetite in the two complexes exhibits extremely low REE concentrations. This is attributable to the fact that the REE partition coefficients of major rock-forming minerals and accessory minerals in both basic and intermediate-acidic rocks are less than 1, causing REEs to preferentially enter the melt phase. With the exception of sample KS4, which displays positive Eu anomalies and negative Ce anomalies (average δEu = 3.19, δCe = 0.52), other samples exhibit negative Eu anomalies and weak positive Ce anomalies (average δEu = 0.74, δCe = 1.13). This indicates that most magnetite was formed after plagioclase crystallization. In an oxidizing environment, Ce^{3+} was oxidized to Ce^{4+}, making it difficult to incorporate it into the magnetite lattice, resulting in severe Ce depletion in sample KS4 (Figure 7A). However, the absence of significant negative Eu anomalies in whole-rock samples suggests that Eu anomalies in magnetite may reflect redox conditions while also indicating the mineral crystallization sequence. Magnetite that crystallizes earlier than plagioclase will not show Eu anomalies, whereas magnetite that crystallizes later than plagioclase will exhibit negative Eu anomalies. The similar REE distribution patterns of monzonite and diorite indicate their close spatial and temporal association. The considerable compositional variation in magnetite in monzonite suggests an extended crystallization history, potentially influenced by magmatic–hydrothermal processes.

The V vs Ti diagram reveals that the V concentration in the Kuangshan complex is lower than that in the Fushan complex, whereas the Ti concentration exhibits minimal variation. There is a continuous change in the compositional characteristics among different lithologies, suggesting that the diorite–monzonite intrusives are the products of fractional crystallization of cognate magma, with the parent magma exhibiting high fO_2 (Yan et al., 1993; Nadoll et al., 2012 Dupuis and Beaudoin, 2011; Figure 15A). The Fushan complex generally has a higher V concentration in magnetite, with no apparent correlation in compositional characteristics among different lithologies, indicating the evolution of non-cognate magma. Fan employed amphibole coexisting with magnetite in the Kuangshan and Fushan complexes as a geothermobarometer to infer the physicochemical conditions of amphibole formation. The average oxygen fugacity of the Kuangshan complex calculated by amphibole is ΔNNO+2.16, and that of the Fushan complex is ΔNNO+1.67 (Fan, 2022). The results calculated by apatite also show that the oxygen fugacity of the Kuangshan complex (ΔFMQ+2.41) is higher than that of the Fushan complex (ΔFMQ+1.77) (Liang et al., 2023). These studies collectively demonstrate that the Kuangshan complex exhibits a higher oxygen fugacity value.

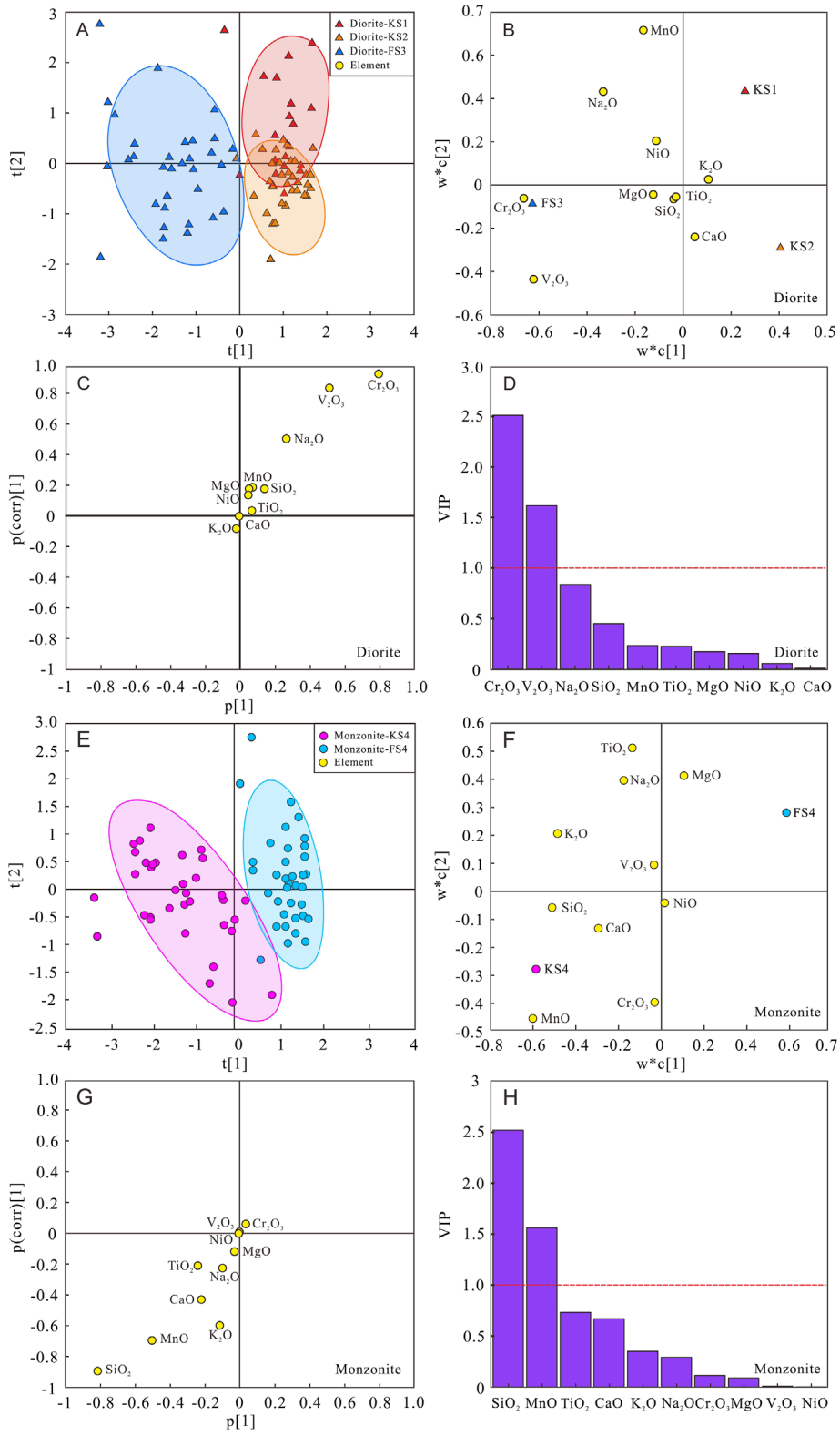

FIGURE 11
PLS-DA and OPLS-DA of magnetite EPMA data in diorite and monzonite within the Kuangshan and Fushan complexes. **(A)** Score plot of diorite. **(B)** Loading plot of diorite. **(C)** S-plot of diorite. **(D)** VIP score plot of diorite. **(E)** Score plot of monzonite. **(F)** Loading plot of monzonite. **(G)** S-plot of monzonite. **(H)** VIP score plot of monzonite.

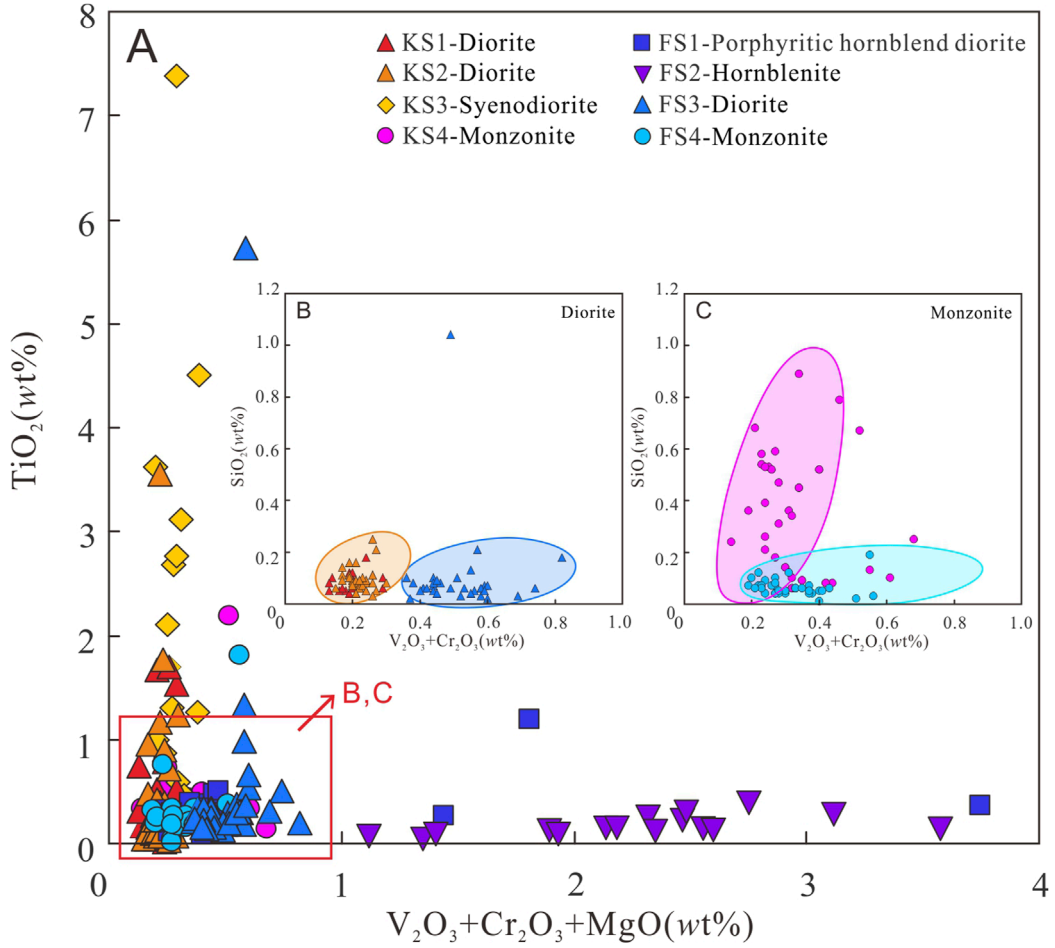

FIGURE 12
Illustration of magnetite metallogenic intensity discrimination in different lithologies. **(A)** Compositional characteristics of magnetite in Kuangshan and Fushan complexes. **(B)** Compositional characteristics of magnetite in diorite. **(C)** Compositional characteristics of magnetite in monzonite.

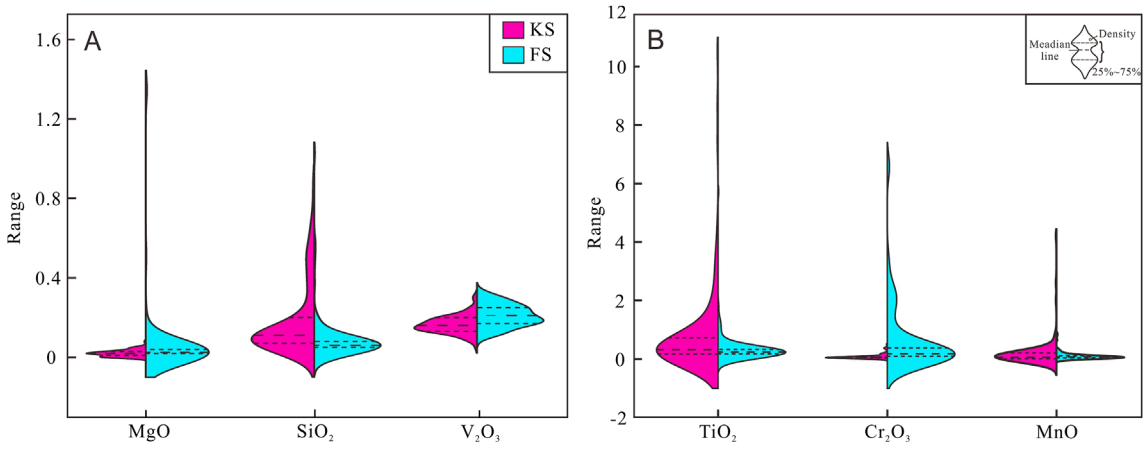

FIGURE 13
Violin plots of characteristic elements of magnetite analyzed by EPMA. **(A)** Violin plots of MgO, SiO2 and V2O3 elements in magnetite. **(B)** Violin plots of TiO2, Cr2O3 and MnO elements in magnetite.

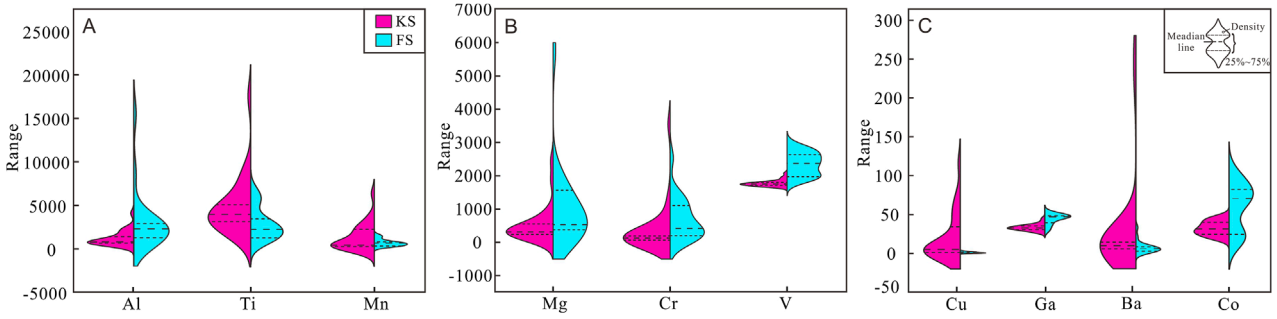

FIGURE 14
Violin plots of characteristic elements of magnetite analyzed by LA–ICP–MS. **(A)** Violin plots of Al, Ti and Mn elements in magnetite. **(B)** Violin plots of Mg, Cr and V elements in magnetite. **(C)** Violin plots of Cu, Ga, Ba and Co elements in magnetite.

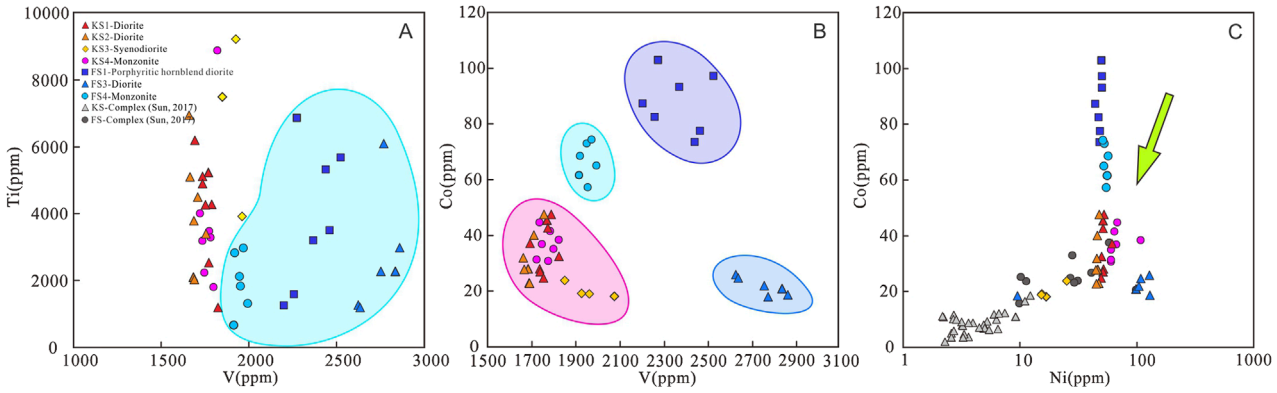

FIGURE 15
Diagram for the relationships of trace elements in magnetite. **(A)** V vs Ti. **(B)** V vs Co. **(C)** Ni vs Co.

In conclusion, the comparative analysis of magnetite composition between the Kuangshan and Fushan complexes reveals that the parent magma of the Kuangshan complex exhibits a higher fO_2, and the magnetite composition characteristics display a continuous evolutionary trend, formed through crystallization differentiation of the parent magma. The parent magma of the Fushan complex has lower fO_2, with the magnetite elements across various lithologies showing no correlation, indicating a discontinuous magmatic evolution. Therefore, it can be inferred that fO_2 is the primary factor controlling the metallogenic intensity in the early-crystallized magnetite.

5.3 Indicative significance of Co mineralization in the Han–Xing-type iron deposit

Co is widely found in the Han–Xing-type iron deposit, and its occurrence state and enrichment mechanisms remain to be elucidated (Qin et al., 2024). Co is a compatible element in magnetite, and the variation in Co concentration within magnetite of different lithologies in ore-forming complexes can provide insights into the enrichment processes of Co in magmatic–hydrothermal systems. This study reveals that the Co concentration in magnetite from the Fushan complex is significantly higher than that in the Kuangshan complex, with substantial compositional variations and no correlation among samples, whereas the Co concentration distribution in magnetite from the Kuangshan complex is relatively concentrated.

Co is a mantle element, and it primarily enters rock-forming and accessory minerals through isomorphic substitution during magmatic crystallization, preferentially incorporating into olivine, followed by pyroxene, ilmenite, and magnetite. The Co concentration in the four minerals formed during the early stages of magmatic crystallization is consistently higher than that those formed during the later stages (Chen et al., 1987). If these minerals crystallize preferentially, the Co concentration in the extension magma will decrease, resulting in lower Co concentration in magnetite. The V vs Co and Co vs Ni diagrams indicate that the parental magma of the Fushan complex exhibited higher Co and Ni concentrations than that of the Kuangshan complex (Figures 15B, C). Magnetite from the Kuangshan and Fushan complexes demonstrates Co depletion while maintaining relatively constant Ni levels, which is attributed to the lower partition coefficient of Co in magnetite compared to Ni, and Co exhibits a higher propensity for migration. This characteristic is particularly

pronounced in the porphyritic hornblende diorite (FS1) and monzonite (FS4) of the Fushan complex, where Co concentrations decrease sharply, indicating that magnetite underwent fractional crystallization during this process (Figure 15C).

The compositional differences in magnetite between the Kuangshan and Fushan complexes indicate that the Co concentration in the Kuangshan complex exhibits relatively minor variations and demonstrates a certain degree of continuity. This phenomenon can be attributed to the substitution reaction between Co and Fe, which is facilitated by the decrease in temperature and pressure during the magmatic evolution process. Co migrates in the form of hydrides, carbonyl hydrides, and carbonyl compounds, resulting in a decrease in the Co content in magnetite (Zheng and Zheng, 2010). The relatively higher Co concentration in magnetite of the Fushan complex suggests a lower abundance of sulfides during this stage, with the low fO_2 environment being unfavorable for Co migration, leading to more Co being hosted in magnetite (Figure 15B). Regarding the formation of the associated Co deposits in the Han–Xing-type skarn iron deposit, the Co concentration in magnetite within the Kuangshan complex indicates that under the early high fO_2 environment, Co^{2+} is oxidized to Co^{3+}, leading to the exsolution and migration of Co from magnetite. This process is particularly conducive to precipitation during the subsequent relatively reduced sulfide stage. The compositional characteristics of magnetite in the Fushan complex indicate that the magma itself may possess a high Co background value. A relatively reducing environment favors the isomorphous substitution of Co^{2+} for Fe^{2+}, enabling Co to enter the magnetite lattice and thereby enhancing Co enrichment in magnetite.

Meanwhile, the author posits that high-Co magnetite provides unique insights into various ore deposit types. For instance, in magmatic copper–nickel sulfide deposits, Co is predominantly located within the sulfides. If the Co concentration in magnetite is high while the concentration of Co in sulfides is low, it may imply a low-sulfur system or incomplete sulfide dissociation. In iron oxide–copper–gold (IOCG) deposits, high Co concentration in magnetite could signify contributions from deep fluids and magma sources. In summary, the elevated Co concentration in magnetite serves as a sensitive indicator of magmatic evolution, the extent of sulfide dissociation, and subsequent hydrothermal activities. This offers valuable insights for studying other ore deposit types, although a comprehensive interpretation requires integration with the geological context, mineral assemblages, and geochemical analyses.

6 Conclusion

(1) With the PLS-DA and OPLS-DA statistical methods, the composition characteristics of magnetite in complexes with different metallogenic intensities are classified and analyzed, thereby establishing a discrimination diagram for strong and weak metallogeny. The magnetite in the Kuangshan complex is rich in Ti, Si, Cu, and Mn, while the magnetite in the Fushan complex is rich in Co, Ni, Cr, and V.

(2) The geochemical research results of magnetite indicate that the Kuangshan and Fushan complexes originate from two distinct metallogenic systems. The Kuangshan complex experienced plagioclase fractional crystallization and formed in a low temperature, high fO_2 environment. The Fushan complex has characteristics of a deep source and was formed in a high temperature, low fO_2 environment.

(3) The changes in the concentrations of Co and Ni in magnetite have certain indicative significance for the mineralization of the Han–Xing-type iron deposit. According to the change in Ti, V, Co, and Ni concentrations, the Kuangshan complex comprises the diorite–monzonite rock mass formed through the crystallization differentiation of cognate magma. The Fushan complex results from the evolution of non-cognate magma. The variation in Co concentration within magnetite in skarn-type deposits is crucial for understanding the migration and precipitation of Co. High fO_2 conditions facilitate the extraction and migration of Co from magnetite, leading to subsequent precipitation during the sulfide phase under reducing environments.

Data availability statement

The original contributions presented in the study are included in the article/Supplementary Material; further inquiries can be directed to the corresponding authors.

Author contributions

JY: Conceptualization, Investigation, Methodology, Visualization, Writing – original draft, Writing – review and editing. WD: Conceptualization, Resources, Supervision, Writing – review and editing. ZJ: Resources, Supervision, Writing – review and editing. ZL: Investigation, Writing – review and editing.

Funding

The author(s) declare that financial support was received for the research and/or publication of this article. This study was funded by the "Geology of Mineral Resources in China" project of the China Geological Survey (grant no. DD20221695, DD20190379, and DD20160346) to Prof. Deng-Hong Wang.

Acknowledgments

The authors are grateful to the associate editor, professor, for providing constructive comments on the manuscript.

Conflict of interest

The authors declare that the research was conducted in the absence of any commercial or financial relationships that could be construed as a potential conflict of interest.

Generative AI statement

The author(s) declare that no Generative AI was used in the creation of this manuscript.

Publisher's note

All claims expressed in this article are solely those of the authors and do not necessarily represent those of their affiliated organizations, or those of the publisher, the editors and the reviewers. Any product that may be evaluated in this article, or claim that may be made by its manufacturer, is not guaranteed or endorsed by the publisher.

Supplementary material

The Supplementary Material for this article can be found online at: https://www.frontiersin.org/articles/10.3389/feart.2025.1567728/full#supplementary-material

References

Bau, M. (1991). Rare-earth element mobility during hydrothermal and metamorphic fluid-rock interaction and the significance of the oxidation state of europium. *Chem. Geol.* 93, 219–230. doi:10.1016/0009-2541(91)90115-8

Buddington, A., and Lindsley, D. (1964). Iron-titanium oxide minerals and synthetic equivalents. *J. Petrology* 5, 310–357. doi:10.1093/petrology/5.2.310

Cai, B. J., Li, X. J., and Wei, S. P. (1987). Feature of the middle ordovician evaporites and its control over the endogenic iron (sulfur) deposits in Han-Xing district, Hebei (in Chinese). *Chin. Acad. Geol. Sci.* 1-84.

Chen, B., Jahn, B. M., Arakawa, Y., and Zhai, M. G. (2004). Petrogenesis of the mesozoic intrusive complexes from the southern Taihang orogen, North China craton: elemental and Sr–Nd–Pb isotopic constraints. *Contributions Mineralogy & Petrology* 148, 489–501. doi:10.1007/s00410-004-0620-0

Chen, B., Tian, W., Jahn, B. M., and Chen, Z. C. (2008). Zircon SHRIMP U–Pb ages and *in-situ* Hf isotopic analysis for the Mesozoic intrusions in South Taihang, North China craton: evidence for hybridization between mantle-derived magmas and crustal components. *Lithos* 102, 118–137. doi:10.1016/J.LITHOS.2007.06.012

Chen, D. Q., and Chen, G. (1990). *Practical rare earth chemistry (in Chinese)*. Beijing: Metallurgical Industry Press, 152–158.

Chen, F. C., Deng, J., Wang, Q. F., Jan Marte, H., Li, G. J., and Gu, Y. W. (2020). LA-ICP-MS trace element analysis of magnetite and pyrite from the Hetaoping Fe-Zn-Pb skarn deposit in Baoshan block, SW China: implications for ore-forming processes. *Ore Geol. Rev.* 117 (2020), 103309. doi:10.1016/j.oregeorev.2020.103309

Chen, G. Y., Sun, D. S., and Yin, H. A. (1987). *Mineralogy and mineral exploration mineralogy (in Chinese)*. Chongqing: Chongqing Press, 1–874.

Dare, S. A. S., Barnes, S. J., and Beaudoin, G. (2012). Variation in trace element content of magnetite crystallized from a fractionating sulfide liquid, Sudbury, Canada: implications for provenance discrimination. *Geochim. Cosmochim. Acta.* 88, 27–50. doi:10.1016/j.gca.2012.04.032

Dare, S. A. S., Barnes, S. J., Beaudoin, G., Méric, A., Boutroy, E., and Potvin-Doucent, C. (2014). Trace elements in magnetite as petrogenetic indicators. *Miner. Deposita.* 49 (7), 785–796. doi:10.1007/s00126-014-0529-0

Deng, X., Li, J., and Wen, G. (2015). U-Pb geochronology of hydrothermal zircons from the early cretaceous iron skarn deposits in the handan-xingtai district, North China craton. *Econ. Geol.* 110, 2159–2180. doi:10.2113/econgeo.110.8.2159

DePaolo, D. J. (1981). Trace element and isotopic effects of combined wallrock assimilation and fractional crystallization. *Earth & Planet. Sci. Lett.* 53 (2), 189–202. doi:10.1016/0012-821X(81)90153-9

Ding, Z. J., Yao, S. Z., Liu, C. Q., Zhou, Z. G., and Yang, M. G. (2003). The dharicdtritlic fethalatim-sadimeelary dops of Dongouba polymetal deposlt: enidence from ore's REE composlton. *Acta Petrol. Sin.* 19 (4), 792–798. doi:10.3321/j.issn:1000-0569.2003.04.022

Dora, M. L., Upadhyay, D., Randive, K. R., Shareef, M., Baswani, S. R., and Ranjan, S. (2020). Trace element geochemistry of magnetite and pyrite and sulfur isotope geochemistry of pyrite and barite from the Thanewasna Cu-(Au) deposit, western Bastar Craton, central India: implication for ore genesis. *Ore Geol. Rev.* 117, 103262. doi:10.1016/j.oregeorev.2019.103262

Dupuis, C., and Beaudoin, G. (2011). Discriminant diagrams for iron oxide trace element fingerprinting of mineral deposit types. *Miner. Deposita* 46, 319–335. doi:10.1007/s00126-011-0334-y

Ewart, A., and Griffin, W. L. (1994). Application of proton microprobe data to trace-element partitioning in volcanic rocks. *Chem. Geol.* 117 (1), 251–284. doi:10.1016/0009-2541(94)90131-7

Fan, L. L. (2022). "The study of Genetic mineralogical of amphibole inMesozoic intrusive rocks in Han-xing area, Southern Hebei Province (in Chinese). *Masters Thesis*. doi:10.27752/d.cnki.gsjzj.2022.000126

Frost, B. R., and Lindsley, D. H. (1991). Chapter 12.OCCURRENCE of IRON-TITANIUM oxides in igneous rocks. *Rev. Mineralogy & Geochem.* 25, 433–468. doi:10.1515/9781501508684-015

Ghaz, J. M., Harris, C., Rahgoshay, M., and Moazzen, M. (2019). Combined igneous and hydrothermal source for the Kiruna-type Bafq magnetite-apatite deposit in Central Iran: trace element and oxygen isotope studies of magnetite. *Ore Geol. Rev.* 105, 590–604. doi:10.1016/j.oregeorev.2019.01.006

Hao, J. J., Shen, J. H., Zhao, X. W., and Feng, D. D. (2011). REE geochemistry of baijian iron deposit in shahe city, Hebei Province. *Geoscience* 25 (03), 545–552. doi:10.1007/s12182-011-0118-0

Hass, J. R., Shock, E. L., and Sassani, D. C. (1995). Rare earth elements in hydrothermal systems: estimates of standard partial modal thermody-namic properties of aqoeous compexes of the rare earth elements at high pressures and temperatures. *Geochim. Cosmochin. Acta* 59 (21), 4329–4350. doi:10.1016/0016-7037(95)00314-P

Huang, X. W., Émilie, B., Sheida, M., Georges, B., Louise, C., and Anthony, F. (2018). Trace element composition of iron oxides from IOCG and IOA deposits: relationship to hydrothermal alteration and deposit subtypes. *Miner. deposita* 54 (4), 525–552. doi:10.1007/s00126-018-0825-1

Huo, Y. A., Su, S. G., Yang, Y. B., and Gu, D. P. (2019). The evidence for lithospheric thinning of Mesozoic North China Craton: taking Guzhen intrusive complex as an example. *Acta Petrol. Sin.* 35, 989–1014. doi:10.18654/1000-0569/2019.04.02

Javad, M. G., Chris, H., Mohammad, R., and Mohssen, M. (2019). Combined igneous and hydrothermal source for the Kiruna-type Bafq magnetite-apatite deposit in Central Iran; Trace element and oxygen isotope studies of magnetite. *Ore Geol. Rev* 105, 590–604. doi:10.1016/j.oregeorev.2019.01.006

Jiang, J. Y., Su, S. G., Cui, X. L., Liu, L. L., Meng, W. Y., and Wang, J. J. (2020). The processes and mechanism of lithospheric thinning in eastern North China craton during early cretaceous: evidence from xishimen complex, Hebei Province. *Acta Petrol. Sin.* 36, 356–390. doi:10.18654/1000-0569/2020.02.03

Jin, Z., Zhang, Z., Hou, T., Santosh, M., and Han, L. (2015). Genetic relationship of high-Mg dioritic pluton to iron mineralization: a case study from the Jinling skarn-type iron deposit in the North China Craton. *J. Asian Earth Sci.* 113, 957–979. doi:10.1016/j.jseaes.2015.03.039

Klinkhammer, G. P., Elderfield, J. M., Edmond, J. M., and Mitra, A. (1994). Geochemical implications of rare earth element patterns in hydrothermal fluids from mid-ocean ridges. *Geochim. Cosmochim. Acta* 58 (23), 5105–5113. doi:10.1016/0016-7037(94)90297-6

Li, D. F., Fu, Y., Sun, X. M., Hollings, P., Liao, J. L., Liu, Q. F., et al. (2018). Corrigendum to "LA-ICP-MS trace element mapping: element mobility of hydrothermal magnetite from the giant Beiya Fe-Au skarn deposit, SW China" [Ore Geol. Rev. 92 (2018) 463–474]. *Ore Geol. Rev.* 95, 1192–1195. doi:10.1016/j.oregeorev.2018.01.005

Li, S. R., and Santosh, M. (2013). Metallogeny and craton destruction: records from the North China craton. *Ore Geol. Rev.* 56, 376–414. doi:10.1016/j.oregeorev.2013.03.002

Li, S. R., Santosh, M., Zhang, H., Shen, J., Dong, G., Wang, J., et al. (2013). Inhomogeneous lithospheric thinning in the central North China Craton: zircon U–Pb and S–He–Ar isotopic record from magmatism and metallogeny in the Taihang Mountains. *Gondwana Res.* 23, 141–160. doi:10.1016/j.gr.2012.02.006

Li, Y. (2019). *Mesozoic magmatism time limit of the South Taihang and its tectonic significance (in Chinese)*. *Masters Thesis*. Shijiazhuang, China: Hebei GEO University.

Liang, X., Wang, F., Zhang, J., Zhang, L., Zhang, J., and Wang, J. (2023). Contraints on petrogenesis and Fe fertility of intrusive complexes in the Han-Xing region, North China Craton from apatite geochemistry. *Minerals* 13 (4), 469. doi:10.3390/min13040469

Liu, Y. J. (1984). *Element geochemistry (in Chinese)*. Beijing: Science Press.

Nadoll, P., Angerer, T., Mauk, J. L., French, D., and Walshe, J. (2014). The chemistry of hydrothermal magnetite: a review. *Ore Geol. Rev.* 61, 1–32. doi:10.1016/j.oregeorev.2013.12.013

Nadoll, P., Mauk, J. L., Hayes, T. S., Koenig, A., and Box, S. (2012). Geochemistry of magnetite from hydrothermal ore deposits and host rocks of the mesoproterozoic belt supergroup, United States. *Econ. Geol.* 107, 1275–1292. doi:10.2113/econgeo.107.6.1275

Nadoll, P., Mauk, J. L., Leveille, R. A., and Koeniget, A. E. (2015). Geochemistry of magnetite from porphyry Cu and skarn deposits in the southwestern United States. *Miner. Deposita* 50, 493–515. doi:10.1007/s00126-014-0539-y

Nielsen, R. L., Forsythe, L. M., Gallahan, W. E., and Fisk, M. R. (1994). Major and trace element magnetite-melt equilibria. *Chem. Geol.* 117, 167–191. doi:10.1016/0009-2541(94)90127-9

Niu, S. Y., Dong, G. R., and Xu, C. S. (1995). The origin and source of magma in the Taihangshan tectono-magmatic belt (in Chinese). *Geol. Rev.* 41 (4), 301–310. doi:10.16509/j.georeview.1995.04.002

Peng, T., Wang, Y., Fan, W., Guo, F., and Peng, B. (2004). SHRIMP zircon U-Pb geochronology of the diorites for southern Taihang Mountains in the North China Interior and its petrogenesis (in Chinese). *Acta Petrol. Sin.* 5, 264–273. doi:10.3321/j.issn:1000-0569.2004.05.020

Qian, Q., and Hermann, J. (2010). Formation of high-Mg diorites through assimilation of peridotite by monzodiorite magma at crustal depths. *J. Petrol.* 51, 1381–1416. doi:10.1093/petrology/egq023

Qin, C., Zhang, J. Q., Masroor, A., Tang, Y. Y., Bai, M., Dong, L. S., et al. (2024). Occurrence characteristics and enrichment mechanism of cobalt in pyrite from the Han-Xing type skarn iron deposit using laser-ablation inductively-coupled-plasma mass-spectrometry elemental mapping, Taihang Mountain, China. *Geol. J.* 59, 1–23. doi:10.1002/gj.5034

Ramdohr, P. (1980). *The ore minerals and their intergrowths*. New York: Pergamon Press, 11–207. doi:10.1180/minmag.1982.046.338.24

Schock, H. H. (1979). Distribution of rare-earth and other trace elements in magnetites. *Chem. Geol.* 26, 119–133. doi:10.1016/0009-2541(79)90034-2

Shen, B. F., Lu, S. N., Zhai, A. M., Li, Z. H., and Yu, E. Z. (1979). The chemical composition characteristics and geological significance of magnetite in contact-metasomatic iron ore deposits in Southern Hebe (in Chinese). *Geol. Rev.* 1, 10–18. doi:10.16509/j.georeview.1979.01.003

Shen, J. F., Li, S. R., Santosh, M., Dong, G., Wang, Y., Liu, H., et al. (2015). Zircon U–Pb geochronology of the basement rocks and dioritic intrusion associated with the Fushan skarn iron deposit, southern Taihang Mountains, China. *J. Asian Earth Sci.* 113, 1132–1142. doi:10.1016/j.jseaes.2015.01.009

Shen, J. F., Santosh, M., Li, S. R., Zhang, H., Yin, N., Dong, G., et al. (2013). The Beiminghe skarn iron deposit, eastern China: geochronology, isotope geochemistry and implications for the destruction of the North China Craton. *Lithos* 156-159, 218–229. doi:10.1016/j.lithos.2012.11.003

Sun, S. S., and Mcdonough, W. F. (1989). "Chemical and isotopic systematics of oceanic basalts: implications for mantle composition and processes,", 42. *Geological Society London*, 313–345. doi:10.1144/GSL.SP.1989.042.01.19

Sun, Y. (2016). *Petrogenesis and mineralization of the early cretaceous intrusive rocks in handan-xingtai area, Hebei province, China, Ph.D (in Chinese). Masters thesis*. Wuhan, China: China University of Geosciences. doi:10.27493/d.cnki.gzdzy.2020.000219

Sun, Y., Wu, T., Xiao, L., Bai, M., and Zhang, Y. (2019). U-Pb ages, Hf-O isotopes and trace elements of zircons from the ore-bearing and ore-barren adakitic rocks in the Handan-Xingtai district: implications for petrogenesis and iron mineralization. *Ore Geol. Rev.* 104, 14–25. doi:10.1016/j.oregeorev.2018.10.010

Sun, Y., Xiao, L., Zhan, Q., Wu, J., Zhu, D., Huang, W., et al. (2015). Petrogenesis of the kuangshancun and hongshan intrusive complexes from the handan–xingtai district: implications for iron mineralization associated with mesozoic magmatism in the North China craton. *J. Asian Earth Sci.* 113, 1162–1178. doi:10.1016/j.jseaes.2015.08.003

Wang, S. J. (1987). *On the typological characteristics of magnetite (in Chinese)*. Wuhan: China University of Geosciences Press.

Wang, Y., Fan, W., Zhang, H., and Peng, T. (2006). Early cretaceous gabbroic rocks from the Taihang mountains: implications for a paleosubduction-related lithospheric mantle beneath the central North China craton. *Lithos* 86, 281–302. doi:10.1016/j.lithos.2005.07.001

Wei, H. F. (2011). *Geological characteristics and genesis of Xishimen skarn iron deposit in Handan (in Chinese). Masters Thesis*. Shijiazhuang, China: Shijiazhuang University of Economics.

Wen, G., Li, J., Hofstra, A. H., Koenig, A. E., and Cui, B. (2020). Textures and compositions of clinopyroxene in an Fe skarn with implications for ore-fluid evolution and mineral-fluid REE partitioning. *Geochimica Cosmochimica Acta* 290, 104–123. doi:10.1016/j.gca.2020.08.020

Wu, F. Y., Yang, J. H., Xu, Y. G., Wilde, S. A., and Walker, R. J. (2019). Destruction of the North China craton in the mesozoic. *Annu. Rev. Earth Planet. Sci.* 47, 173–195. doi:10.1146/annurev-earth-053018-060342

Xu, W. L., Yang, D. B., Gao, S., Pei, F. P., and Yu, Y. (2010). Geochemistry of peridotite xenoliths in Early Cretaceous high-Mg# diorites from the Central Orogenic Block of the North China Craton: the nature of Mesozoic lithospheric mantle and constraints on lithospheric thinning. *Chem. Geol.* 270, 257–273. doi:10.1016/j.chemgeo.2009.12.006

Yan, B. Q., Wu, K. L., and Wang, W. T. (1993). The genesis mineralogical characteristics of magnetite in the Zhangzhou complex rock mass, Fujian Province. *Geol. Fujian* 12, 1–16.

Yang, F. Q., Mao, J. w., Xu, L. G., Zhang, Y., Liu, F., Hung, C. L., et al. (2007). REE geochemiktry of the Mengku iron deposit, Xinjiang and its indication for iron mineraliafion (in Chinese). *Acta Petrol. Sin.* 23 (10), 2443–2456. doi:10.3969/j.issn.1000-0569.2007.10.013

Yang, Y. B., Su, S. G., Huo, Y. A., Ning, Y. G., and Gu, D. P. (2022). Formation mechanism of Hanxing type iron deposit: evidence from the iron-bearing melt-fluid assemblage in porphyritic monzonite from Wu'an, Hebei Province. *Earth Sci. Front.* 29, 304–318. doi:10.13745/j.esf.sf.2021.7.22

Ye, Q. T. (1982). Typomorphic characteristics and genesis significance of magnetite from some iron ore deposita in eastern Guangdong (in Chinese). *Rock Mineral Analysis* 1, 44–51.

Zhang, J. Q., Li, S. R., Santosh, M., Wang, J. Z., and Li, Q. (2015). Mineral chemistry of high-Mg diorites and skarn in the Han-Xing Iron deposits of South Taihang Mountains, China: constraints on mineralization process. *Ore Geol. Rev.* 64, 200–214. doi:10.1016/j.oregeorev.2014.07.007

Zhang, J. Q., Wang, J. Z., Li, S. R., Shen, J. F., and Lu, J. (2018). Genetic mineralogy analysis on the mineralization process of skarn iron deposit in han-xing area, southern Taihang mountains (in Chinese). *Petrology Geochem.* 37, 205–213+371. doi:10.19658/j.issn.1007-2802.2018.37.023

Zhang, J. Q., Yan, L., Santosh, M., Li, S., Lu, J., Wang, D., et al. (2020). Tracing the genesis of skarn-type iron deposit in central North China Craton: insights from mineral zoning textures in ore-forming intrusion. *Geol. J.* 55, 6280–6295. doi:10.1002/gj.3800

Zhang, Z. C., Hou, T., Santosh, M., Li, H., Li, J. W., Zhang, Z. H., et al. (2014). Spatio-temporal distribution and tectonic settings of the major iron deposits in China: an overview. *Ore Geol. Rev.* 57, 247–263. doi:10.1016/j.oregeorev.2013.08.021

Zhao, J. S., Qiu, X. L., Zhao, B., Xu, X. L., Yu, Y., and Lu, T. S. (2007). REE geochemstry of mineralized skarns from Daye to Wushan region, China. *Geochem. J.* 04, 400–412. doi:10.19700/j.0379-1726.2007.04.010

Zheng, D. Z., and Zheng, R. F. (2010). Migration forms and ore-forming mechanism for cobalt (in Chinese). *Acta Geol. Sichuan* 30, 364–368. doi:10.3969/j.issn.1006-0995.2010.03.029

Zheng, J. M., Chen, M. H., Xu, L. G., Gao, J. J., Hu, Y. Y., and Liang, Z. H. (2006). Characteristics of structurally controlled skarn iron deposits and prospecting targets in Handan-Xingtai area (in Chinese). *Mineral. Deposits* 25, 115–118.

Zhu, R. X., Yang, J. H., and Wu, F. Y. (2012). Timing of destruction of the North China craton. *Lithos* 149, 51–60. doi:10.1016/j.lithos.2012.05.013